An isogeometric boundary element method for electromagnetic scattering with compatible B-spline discretizations

R. N. Simpson[a,*], Z. Liu[a], R. Vázquez[b,c], J.A. Evans[d]

[a]*School of Engineering, University of Glasgow, Glasgow G12 8QQ, U.K.*
[b]*Institute of Mathematics, École Polytechnique Fédérale de Lausanne, Station 8, 1015 Lausanne, Switzerland*
[c]*Istituto di Matematica Applicata e Tecnologie Informatiche "E. Magenes" del CNR, via Ferrata 5, 27100, Pavia (Italy)*
[d]*Department of Aerospace Engineering Sciences, University of Colorado Boulder, Boulder, CO 80305, USA*

Abstract

We outline the construction of compatible B-splines on 3D surfaces that satisfy the continuity requirements for electromagnetic scattering analysis with the boundary element method (method of moments). Our approach makes use of Non-Uniform Rational B-splines to represent model geometry and compatible B-splines to approximate the surface current, and adopts the isogeometric concept in which the basis for analysis is taken directly from CAD (geometry) data. The approach allows for high-order approximations and crucially provides a direct link with CAD data structures that allows for efficient design workflows. After outlining the construction of div- and curl-conforming B-splines defined over 3D surfaces we describe their use with the electric and magnetic field integral equations using a Galerkin formulation. We use Bézier extraction to accelerate the computation of NURBS and B-spline terms and employ $\mathscr{H}$-matrices to provide accelerated computations and memory reduction for the dense matrices that result from the boundary integral discretization. The method is verified using the well known Mie scattering problem posed over a perfectly electrically conducting sphere and the classic NASA almond problem. Finally, we demonstrate the ability of the approach to handle models with complex geometry directly from CAD without mesh generation.

Keywords: electromagnetic scattering, compatible B-splines, isogeometric

analysis, boundary element method, method of moments

1. Introduction

Research into unifying geometry and analysis for efficient design workflows has progressed rapidly in recent years driven by the isogeometric analysis and computational geometry research communities. Analysis based on geometry discretizations now covers a wide range of technologies including NURBS [1], T-splines [2], LR B-splines [3], PHT-splines [4] and subdivision surfaces [5]. A major research challenge at present is the automatic generation of volumetric discretizations from given geometric surface data and promising research includes the work of [6, 7] based on T-splines. In contrast, analysis methods based on shell formulations or boundary integral methods are known to require only a surface discretization exhibiting key benefits for a common geometry and analysis model since no additional volumetric processing is required. There has been much research into isogeometric shell formulations including [5, 8, 9] and developments into isogeometric boundary element methods based on NURBS [10, 11], T-splines [12, 13] and subdivision surfaces [14].

A key application of the boundary element method is the analysis of electromagnetic scattering over complex geometries in which a perfectly electrically conducting (PEC) assumption can be made. The method is often termed the method of moments within the electromagnetic research community but is synonymous with the Galerkin boundary element method. It is well known that a straightforward application of nodal basis functions to the electric and magnetic field integral equations (EFIE, MFIE) prevents numerical convergence and instead, discrete spaces that satisfy the relevant continuity requirements must be used. The most commonly used discretization that satisifes the relevant continuity requirements are Raviart-Thomas [15] or RWG [16] basis functions that are mainly based on low order polynomials.

In the context of isogeometric analysis progress has been made on the development of spline-based compatible discretizations [17, 18, 19, 20] in which

*Corresponding author
Email address: robert.simpson.2@glasgow.ac.uk (R. N. Simpson)

a discrete de Rham sequence can be constructed providing a crucial step towards application of isogeometric analysis for fluid flow and electromagnetics applications. This fundamental work opens up the opportunity for the development of an isogeometric boundary element method (isogeometric method of moments) for electromagnetic scattering which is the focus of the present study. We note similar work in which subdivision surfaces are employed [21], but we believe that use of B-spline based algorithms provides greater refinement flexibility, provide a natural link with NURBS based systems that are ubiquitous in modern engineering design software, and offer higher convergence rates over equivalent subdivision schemes with extraordinary points.

We organise the paper as follows: first, we prescribe the Galerkin formulation of the relevant integral equations that govern electromagnetic scattering; we give an overview of NURBS surfaces and detail the construction of compatible B-splines; we then specify the fully discretized form of the integral equations for electromagnetic scattering with compatible B-splines; we cover implementation details of the method including fast evaluation of basis functions through Bézier extraction and the use of $\mathscr{H}$-matrices to approximate dense matrices; we verify the present method by performing electromagnetic scattering over a sphere in which a closed-form solution is provided by Mie scattering theory and finally, we demonstrate the ability of the present approach to perform electromagnetic scattering of PEC bodies with complex geometries taken directly from CAD software. It is assumed that time-harmonic fields are prescribed and, unless stated otherwise, it can be assumed that $\mathbf{x} \in \mathbb{R}^3$.

2. Electric field integral equation: Galerkin formulation

We first assume a PEC domain Ω with connected boundary $\Gamma := \partial\Omega$ residing within an unbounded domain Ω_∞ with isotropic permeability and permittivity given by the scalar quantities ε and μ respectively. We further assume a polarized time-harmonic electromagnetic plane wave of angular frequency ω is imposed on the PEC body with a wavenumber $k = \omega\sqrt{\varepsilon\mu}$. Denoting $\mathbf{E}$ as the total electric field, in the presence of an electromagnetic wave a surface current $\mathbf{J}$ is induced and the following PEC condition holds on the surface of the scattered object

$$\mathbf{n} \times \mathbf{E} = 0 \tag{1}$$

where $\mathbf{n}$ represents the outward pointing normal vector. We specify the incident wave as $\mathbf{E}^i(\mathbf{x}) = \mathbf{p}\, e^{-jk\mathbf{d}\cdot\mathbf{x}}$ where j is the unit imaginary number, $\mathbf{p} = (p_x, p_y, p_z)$ is a polarization vector and $\mathbf{d} = (d_x, d_y, d_z), |\mathbf{d}| = 1$ is a propagation vector. The relationship between the total, incident and scattered electric fields is written as

$$\mathbf{E} = \mathbf{E}^i + \mathbf{E}^s \tag{2}$$

where $\mathbf{E}^s$ represents the scattered electric field. The entire set-up is depicted in Figure 1.

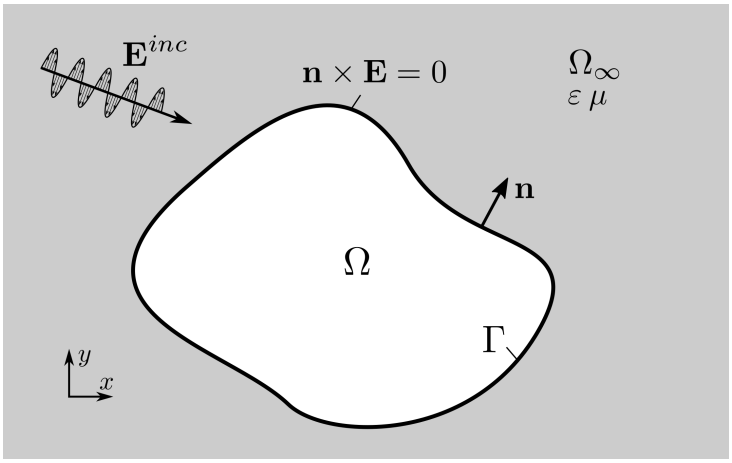

Figure 1: A PEC domain residing within an infinite domain impinged by an electromagnetic plane wave.

Following the potential formulation of Maxwell's equations (see e.g. [22]), the scattered electric field can be expressed in terms of an electric potential φ and magnetic vector potential $\mathbf{A}$ (assuming time-harmonic fields) as

$$\mathbf{E}^s = -j\omega\mathbf{A} - \nabla\varphi \tag{3}$$

where the electric potential is given by

$$\varphi(\mathbf{x}) = \frac{1}{\varepsilon}\int_\Gamma \rho\, \frac{e^{-jkr}}{4\pi r}\, \mathrm{d}\Gamma(\mathbf{y}) \tag{4}$$

with $r := |\mathbf{x} - \mathbf{y}|$ and the charge density ρ expressed as

$$\rho = -\frac{1}{j\omega}\nabla \cdot \mathbf{J} \tag{5}$$

with the magnetic potential related to the surface current through

$$\mathbf{A}(\mathbf{x}) = \mu \int_{\Gamma} \mathbf{J}(\mathbf{y}) \, \frac{e^{-jkr}}{4\pi r} \, \mathrm{d}\Gamma(\mathbf{y}). \tag{6}$$

We omit variable dependencies in future equations where they are implied by their context and adopt the notation $\Gamma_y \equiv \Gamma(\mathbf{y})$ and $\Gamma_x \equiv \Gamma(\mathbf{x})$. Substituting (4) and (6) into (3) and employing (5) with $k^2 = \omega^2 \varepsilon \mu$ and $j^2 = -1$, the scattered electric field is expressed in terms of surface quantities as

$$\mathbf{E}^s = -j\omega\mu \left(\int_{\Gamma_y} \mathbf{J} \frac{e^{-jkr}}{4\pi r} \, \mathrm{d}\Gamma_y + \frac{1}{k^2} \nabla_{\Gamma_x} \int_{\Gamma_y} \nabla_{\Gamma_y} \cdot \mathbf{J} \, \frac{e^{-jkr}}{4\pi r} \, \mathrm{d}\Gamma_y \right) \tag{7}$$

where ∇_{Γ_x}, ∇_{Γ_y} are surface gradient operators taken with respect to $\mathbf{x}$ and $\mathbf{y}$ respectively. Defining the linear operator

$$L^E[\boldsymbol{\tau}(\mathbf{x})] = \int_{\Gamma_y} \boldsymbol{\tau} \frac{e^{-jkr}}{4\pi r} \, \mathrm{d}\Gamma_y + \frac{1}{k^2} \nabla_{\Gamma_x} \int_{\Gamma_y} \nabla_{\Gamma_y} \cdot \boldsymbol{\tau} \, \frac{e^{-jkr}}{4\pi r} \, \mathrm{d}\Gamma_y \tag{8}$$

along with the force term $\mathbf{f} = (j\omega\mu)^{-1} \mathbf{E}^i$, the Galerkin formulation of the EFIE reads as:

given $\mathbf{f}$, find $\mathbf{J} \in \mathcal{V}$ such that

$$\langle \mathbf{w}, L^E[\mathbf{J}] \rangle = \langle \mathbf{w}, \mathbf{f} \rangle \quad \forall \, \mathbf{w} \in \mathcal{V} \tag{9}$$

where $\mathcal{V}$ is the trace space $H^{-\frac{1}{2}}(\mathrm{div}_\Gamma, \Gamma)$, and the $\langle \cdot, \cdot \rangle$ is the duality pairing between $\mathcal{V}$ and $H^{-\frac{1}{2}}(\mathrm{curl}_\Gamma, \Gamma)$. When the fields are smooth enough, the duality pairing reduces to $\langle \mathbf{u}, \mathbf{v} \rangle = \int_\Gamma \mathbf{u} \cdot \mathbf{v} \, \mathrm{d}\Gamma$.

We define the finite dimensional subspace $\mathcal{V}_h \subset \mathcal{V}$ which allows the solution of (9) to be approximated as the solution of

given $\mathbf{f}$, find $\mathbf{J}_h \in \mathcal{V}_h$ such that

$$\langle \mathbf{w}_h, L^E[\mathbf{J}_h] \rangle = \langle \mathbf{w}_h, \mathbf{f} \rangle \quad \forall \, \mathbf{w}_h \in \mathcal{V}_h. \tag{10}$$

Conventionally, $\mathbf{w}_h$ and $\mathbf{J}_h$ are discretized through the Raviart-Thomas basis, but in our approach we make use of compatible B-splines that we now outline in detail.

3. Discretization

3.1. NURBS surfaces

Our implementation assumes a watertight NURBS surface parameterization that may be composed of multiple patches and we further assume that the connectivity of global basis functions between NURBS patches is known *a priori*. Dealing with the single patch case first, a NURBS surface parameterization is defined through a set of four-dimensional homogeneous control points $\{\mathbf{P}_a\}_{a=1}^{n_p}$, $\mathbf{P}_a = (x_a w_a, y_a w_a, z_a w_a, w_a)$ (where w_a represents a control point weight), a set of knot vectors $\{\Xi_i\}_{i=1}^{2}$ where $\Xi_1 = \{0 = s_1, s_2, \ldots, s_{n+p+1} = 1\}$, $\Xi_2 = \{0 = t_1, t_2, \ldots, t_{m+q+1} = 1\}$ and a degree vector $\mathbf{p} = (p, q)$. n and m denote the number of basis functions defined through the knot vectors Ξ_1 and Ξ_2 respectively with $n_p = n \times m$. We assume all knot vectors are open (i.e. for a given degree p the knot vector contains $p+1$ equal knot values at its beginning and end).

Defining the parametric domain $\widehat{\Gamma} = (0, 1)^2 \subset \mathbb{R}^2$ and physical domain $\Gamma \subset \mathbb{R}^3$, a NURBS geometric mapping $\mathbf{F} : \widehat{\Gamma} \to \Gamma$ can be written in terms of parametric coordinates $\mathbf{s} = (s, t) \in \widehat{\Gamma}$ as

$$\mathbf{F} = \sum_{a=1}^{n_p} R_a(\mathbf{s}) \mathbf{P}_a \tag{11}$$

with the set of rational basis functions $\{R_a\}_{a=1}^{n_p}$ defined as

$$R_a(\mathbf{s}) \equiv R_a(s, t) = \frac{w_a B_a(s, t)}{\sum_{b=1}^{nm} w_b B_b(s, t)} \quad a = 1, 2, \ldots n_p \tag{12}$$

where

$$B_a(s, t) = B_i^p(s) B_j^p(t),$$

with the set of univariate B-spline basis functions $\{B_i^p\}_{i=1}^{n}$ defined through the Cox-de-Boor algorithm (see e.g. [23]). The parametric basis function index a is defined in terms of the univariate basis indices i, j through

$$a = (j - 1)n + i. \tag{13}$$

Defining vectors of unique knot values in the s and t parametric directions as $\boldsymbol{\zeta}_1 = \{\zeta_1^1, \zeta_2^1, \ldots \zeta_{n_k}^1\}$ and $\boldsymbol{\zeta}_2 = \{\zeta_1^2, \zeta_2^2, \ldots \zeta_{m_k}^2\}$ respectively, the mesh in the parametric domain is given by

$$\mathcal{M}_h = \{Q = (\zeta_i^1, \zeta_{i+1}^1) \times (\zeta_j^2, \zeta_{j+1}^2),\ 1 \leq i \leq n_k - 1,\ 1 \leq j \leq m_k - 1\} \tag{14}$$

with $n_e = \text{size}(\mathcal{M}_h)$ denoting the number of elements within the patch. Each element Q within the patch contains $(p+1)\times(q+1)$ non-zero basis functions.

3.2. Compatible B-spline approximation

Given a set of univariate B-spline basis functions $\{B_i^p\}_{i=1}^n$, the space spanned by this basis is defined as

$$\widehat{S}^p := \text{span}\{B_i^p\}_{i=1}^n \tag{15}$$

and in a similar manner, the tensor product B-spline space defined through the set of B-spline basis functions $B_a := B_i^p \otimes B_j^q,\ i = 1, 2, \ldots, n,\ j = 1, 2, \ldots m$ is defined as

$$\widehat{S}^{p,q} := \widehat{S}^p \otimes \widehat{S}^q = \text{span}\{B_a\}_{a=1}^{n_b} \tag{16}$$

where the mapping defined by (13) is employed and a hat symbol denotes that the quantity is defined over the parametric domain. A div-conforming vector B-spline space is defined over the parametric domain as

$$\widehat{S}_1 := \widehat{S}^{p,q-1} \times \widehat{S}^{p-1,q} \tag{17}$$

and likewise, a curl-conforming vector B-spline space is defined as

$$\widehat{S}_2 := \widehat{S}^{p-1,q} \times \widehat{S}^{p,q-1}. \tag{18}$$

The equivalent div-conforming and curl-conforming spaces defined in the physical domain are then constructed through appropriate Piola mappings as

$$\mathcal{U}_h = \{\mathbf{u} : \mathbf{u} \circ \mathbf{F} = \frac{1}{J} D\mathbf{F}\, \widehat{\mathbf{u}},\ \widehat{\mathbf{u}} \in \widehat{S}_1\} \tag{19}$$

and

$$\mathcal{V}_h = \{\mathbf{v} : \mathbf{v} \circ \mathbf{F} = \left(D\mathbf{F}^+\right)^{\mathrm{T}}\, \widehat{\mathbf{v}},\ \widehat{\mathbf{v}} \in \widehat{S}_2\} \tag{20}$$

respectively, where $D\mathbf{F}$ is the Jacobian associated with the geometric mapping $\mathbf{F}$ which for 3D surfaces is given by the rectangular matrix

$$D\mathbf{F} = \begin{bmatrix} \frac{\partial x}{\partial s} & \frac{\partial x}{\partial t} \\ \frac{\partial y}{\partial s} & \frac{\partial y}{\partial t} \\ \frac{\partial z}{\partial s} & \frac{\partial z}{\partial t} \end{bmatrix}, \tag{21}$$

$D\mathbf{F}^+$ is the Monroe-Penrose pseudoinverse of the Jacobian given by

$$D\mathbf{F}^+ = \left(D\mathbf{F}^T D\mathbf{F}\right)^{-1} D\mathbf{F}^T, \tag{22}$$

and J is the surface element given by

$$J = \sqrt{\left(\frac{\partial y}{\partial s}\frac{\partial z}{\partial t} - \frac{\partial z}{\partial s}\frac{\partial y}{\partial t}\right)^2 + \left(\frac{\partial z}{\partial s}\frac{\partial x}{\partial t} - \frac{\partial x}{\partial s}\frac{\partial z}{\partial t}\right)^2 + \left(\frac{\partial x}{\partial s}\frac{\partial y}{\partial t} - \frac{\partial y}{\partial s}\frac{\partial x}{\partial t}\right)^2}. \tag{23}$$

Further details of the derivation of (19) and (20) can be found in [18, 20] and the derivation of (21)-(23) can be found in [24, Sect. 5.4].

3.2.1. Basis functions

Expressing vectors within the parametric domain as $\widehat{\mathbf{v}} = \widehat{v}_i \widehat{\mathbf{e}}_i$, $i = 1, 2$ and adopting the notation $\{B_a^{(p,q-1)}\}_{a=1}^{n_b^1}$, $\{B_a^{(p-1,q)}\}_{a=1}^{n_b^2}$ to represent the set of B-spline basis functions associated with the spaces $\widehat{S}^{p,q-1}$ and $\widehat{S}^{p-1,q}$ respectively, the set of div-conforming basis functions in the parametric domain $\hat{\Gamma}$ is defined as

$$\widehat{\mathbf{N}}_a^{\mathrm{div}}(s,t) = \begin{cases} B_a^{(p,q-1)}(s,t)\,\widehat{\mathbf{e}}_1 & 1 \le a \le n_b^1 \\ B_{a-n_b^1}^{(p-1,q)}(s,t)\,\widehat{\mathbf{e}}_2 & n_b^1 + 1 \le a \le n_b^1 + n_b^2 \end{cases} \tag{24}$$

which are transformed into a set of div-conforming basis functions on the surface Γ using the Piola transformation defined in (19) as

$$\mathbf{N}_a^{\mathrm{div}}(\mathbf{x}(s,t)) = \frac{1}{J} D\mathbf{F}\, \widehat{\mathbf{N}}_a^{\mathrm{div}}(s,t) \quad 1 \le a \le n_b = n_b^1 + n_b^2 \tag{25}$$

where $\mathbf{F} \equiv \mathbf{F}(s,t)$ is implied. Curl-conforming basis functions are defined in analogous fashion.

Global div- and curl-conforming approximations in physical space can then simply be expressed through

$$\mathbf{u}_h^{\mathrm{div}}(\mathbf{x}) = \sum_{a=1}^{n_b} \mathbf{N}_a^{\mathrm{div}}(\mathbf{x}) u_a \tag{26}$$

and

$$\mathbf{v}_h^{\mathrm{curl}}(\mathbf{x}) = \sum_{a=1}^{n_b} \mathbf{N}_a^{\mathrm{curl}}(\mathbf{x}) v_a \tag{27}$$

respectively, where u_a and v_a are control coefficients. To illustrate the construction of compatible B-splines based on the NURBS parameterization shown in Figure 2, the bivariate B-splines generated from univariate B-splines are shown for two example basis functions in Figure 3. Further application of the Piola transformation as defined in (25) generates the div-conforming B-spline basis functions in physical space as shown in Figure 4.

Remark 1. *For simplicity the construction of compatible B-splines is described using the same degree (p, q) of the geometry. In practice it is possible to use a different degree for the B-splines discretization, as we will see in the numerical experiments.*

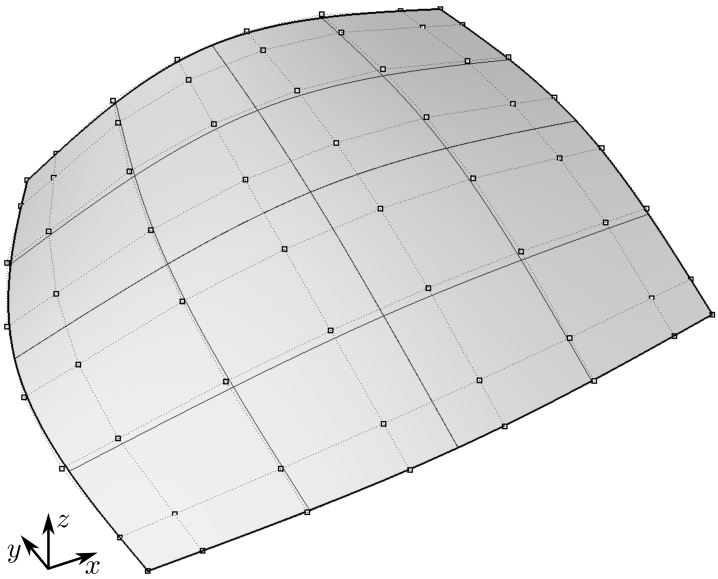

Figure 2: Bicubic NURBS patch defined by $n_{cp} = 64$ control points, knot vectors $\Xi_1 = \Xi_2 = \{0, 0, 0, 0, \frac{1}{4}, \frac{1}{2}, \frac{1}{2}, \frac{3}{4}, 1, 1, 1, 1\}$ and degrees $p = q = 3$. The degrees and knot vectors defined by the geometry are used directly to construct div-conforming B-splines.

3.3. Multipatch discretizations

Invariably, NURBS surfaces will consist of multiple patches whose union defines the physical domain through

$$\overline{\Gamma} = \bigcup_{i=1}^{n_d} \overline{\Gamma_i} \tag{28}$$

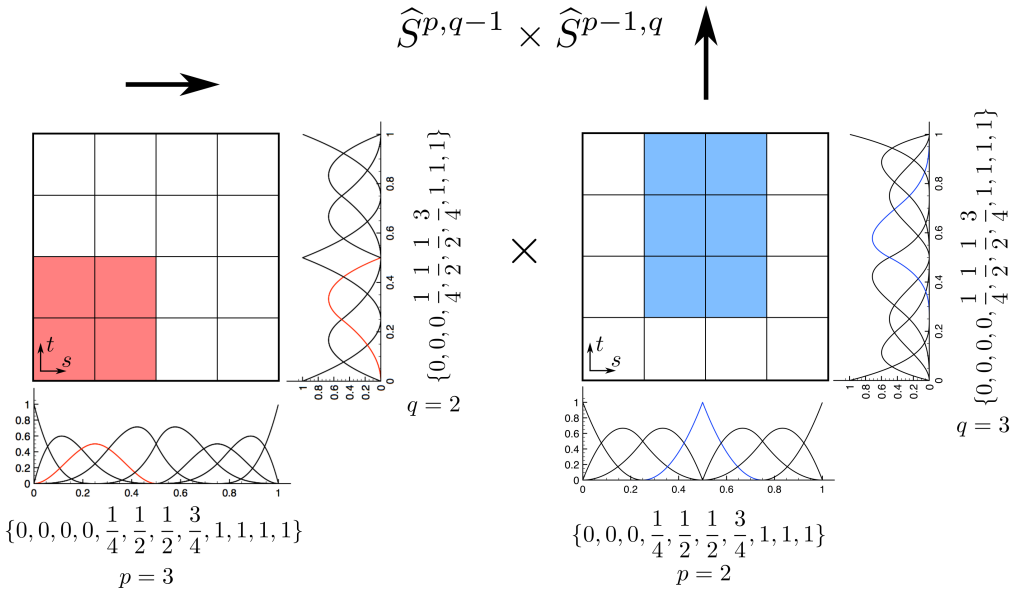

Figure 3: Construction of div-conforming basis functions defined over the parametric domain using the set of knot vectors and degrees defined by the geometry in Figure 2. The basis functions that define $\widehat{\mathbf{N}}_{19}^{\text{div}}(s,t)$ and the parametric interval that defines its span are highlighted in red. Similarly for $\widehat{\mathbf{N}}_{88}^{\text{div}}(s,t)$ where all quantities are highlighted blue.

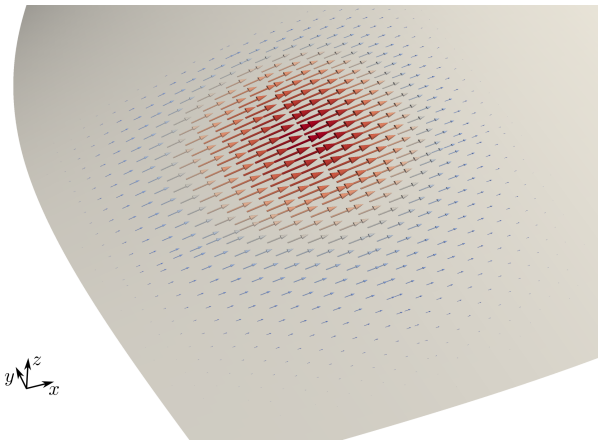

(a) $\mathbf{N}_{19}^{\text{div}}(\mathbf{x})$

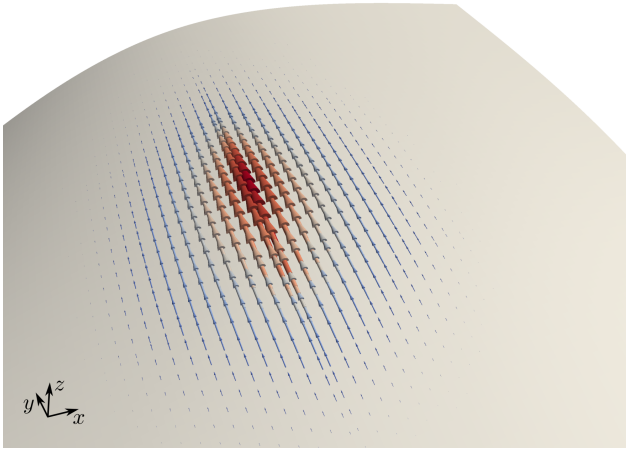

(b) $\mathbf{N}_{88}^{\text{div}}(\mathbf{x})$

Figure 4: Div-conforming B-splines defined over the surface given by the NURBS geometric mapping illustrated in Figure 2. The basis functions correspond to those highlighted in Figure 3 where the Piola transform defined through (19) has been applied.

where n_d is the number of parametric domains or patches and $\Gamma_i \cap \Gamma_j = \emptyset$ for $i \neq j$. Each domain Γ_i is constructed through a NURBS geometric mapping $\mathbf{F}_i : \widehat{\Gamma} \to \Gamma_i$ with parametric coordinates $\mathbf{s} \in \widehat{\Gamma}$ as

$$\mathbf{F}_i = \sum_{a=1}^{n_p^i} R_a^i(\mathbf{s}) \mathbf{P}_a^i \tag{29}$$

where the index i indicates that the relevant quantity is restricted to patch Γ_i. We require for two patches Γ_i and Γ_j with $i \neq j$ and which share a common edge the geometry mapping along the shared edge is the same. In addition, the knot vectors associated with each patch at the common edge must be the same, up to an affine transformation. In practice, this means that at the interface between two patches the parametrization and the meshes must coincide. Figures 5a and 5b illustrate the geometry mappings of a multipatch NURBS geometry and an example mesh respectively.

A global geometry connectivity array C_g can be defined which maps a parametric basis function index a and patch index i to a global geometry basis index as

$$A = C_g(i, a) \quad i = 1, 2 \ldots n_d,\ a = 1, 2, \ldots n_p^i. \tag{30}$$

The definition of the geometry connectivity array and the NURBS parameterization given by (29) allows a multipatch NURBS parameterization to be constructed such as that shown in Figure 5c.

As is well-known with vector bases, care must be taken when constructing global compatible basis functions since both the global basis function index and the orientation sign must be stored and we refer the reader to [25] where div- and curl-conforming B-spline approximations are constructed in a volumetric context. We define the vector basis connectivity for a div-conforming basis through

$$A = C_n(i, a) \quad i = 1, 2 \ldots n_d,\ a = 1, 2, \ldots n_b^i$$

where n_b^i is the number of compatible B-spline basis functions in patch i. This allows a global multipatch compatible B-spline discretization to be written as

$$\mathbf{u}_h^{\mathrm{div}}(\mathbf{x}) = \sum_{A=1}^{N_b} \mathbf{N}_A^{\mathrm{div}}(\mathbf{x}) u_A \tag{31}$$

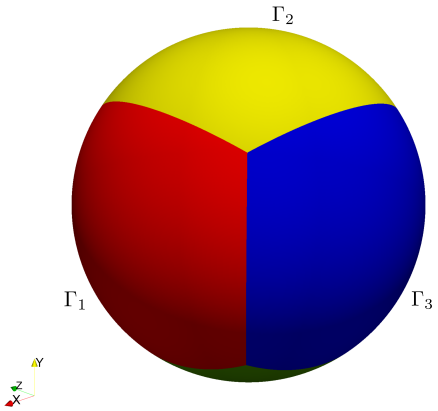

(a) Physical domain Γ.

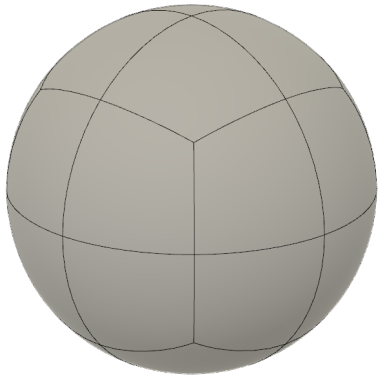

(b) Mesh (one level of h-refinement).

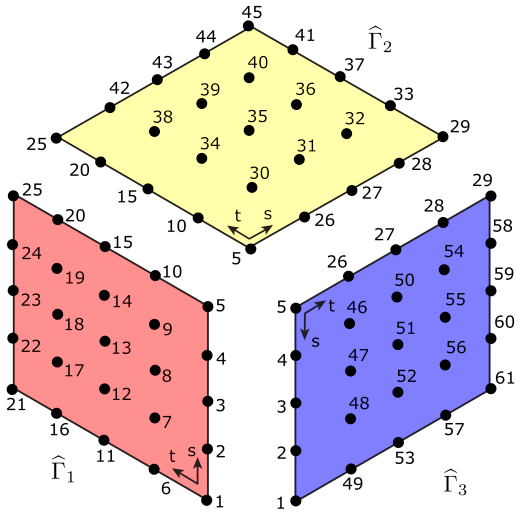

(c) Parametric domains and geometry (nodal) connectivity.

Figure 5: An example multipatch NURBS surface composed of patches of order $(4, 4)$. Both physical and parametric domains are illustrated alongside an example mesh.

where N_b is the global number of basis functions, $\mathbf{N}_A^{\text{div}}|_{\Gamma_i} \equiv \mathbf{N}_{C_n(i,a)}^{\text{div}} \equiv \text{sgn}(i,a)\mathbf{N}_{i,a}^{\text{div}}$.

From an implementation standpoint the main consideration is the construction of the global basis connectivity along the edges of parametric domains, which is best illustrated graphically. Figure 6 shows an example vector basis connectivity for div-conforming B-splines of order $(4,3)\times(3,4)$ based on the geometry of Figure 5. Similar connectivities can be constructed for curl-conforming B-splines.

4. Discretized EFIE with compatible B-splines

In the present work $\mathbf{w}_h$ and $\mathbf{J}_h$ in (10) are defined through the the div-conforming B-spline discretization given by (31) and can be expressed as

$$\mathbf{w}_h(\mathbf{x}) = \sum_{A=1}^{N_b} \mathbf{N}_A^{\text{div}}(\mathbf{x}) w_A \tag{32}$$

$$\mathbf{J}_h(\mathbf{x}) = \sum_{A=1}^{N_b} \mathbf{N}_A^{\text{div}}(\mathbf{x}) j_A. \tag{33}$$

Substituting (32) and (33) into (10) and applying the divergence theorem to transfer a derivative onto $\mathbf{w}_h$, a system of equations is formed as

$$\mathbf{Z}_{AB}\mathbf{J}_B = \mathbf{f}_A \tag{34}$$

where

$$\begin{aligned}\mathbf{Z}_{AB} = \int_{\Gamma_x} \mathbf{N}_A^{\text{div}} \cdot \left(\int_{\Gamma_y} \mathbf{N}_B^{\text{div}} \frac{e^{-jkr}}{4\pi r} \, \mathrm{d}\Gamma_y \right) \mathrm{d}\Gamma_x \\ - \frac{1}{k^2} \int_{\Gamma_x} \nabla_{\Gamma_x} \cdot \mathbf{N}_A^{\text{div}} \left(\int_{\Gamma_y} \nabla_{\Gamma_y} \cdot \mathbf{N}_B^{\text{div}} \frac{e^{-jkr}}{4\pi r} \, \mathrm{d}\Gamma_y \right) \mathrm{d}\Gamma_x\end{aligned} \tag{35}$$

$$\mathbf{f}_A = \frac{1}{j\omega\mu} \int_{\Gamma_x} \mathbf{N}_A^{\text{div}} \cdot \mathbf{E}^i \, \mathrm{d}\Gamma_x \tag{36}$$

and $\mathbf{J}_B$ represents a vector of unknown surface current density coefficients. A similar procedure can be carried out for the magnetic field integral equation as detailed in Appendix A.

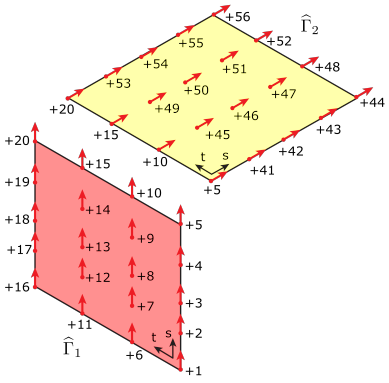

(a) Domains $\widehat{\Gamma}_1$ and $\widehat{\Gamma}_2$.

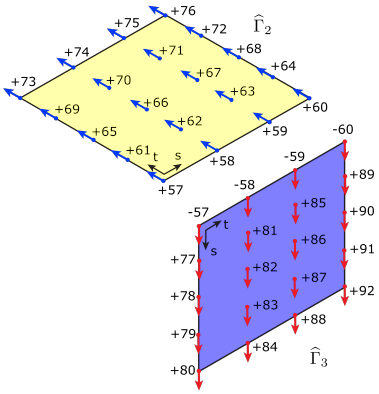

(b) Domains $\widehat{\Gamma}_2$ and $\widehat{\Gamma}_3$.

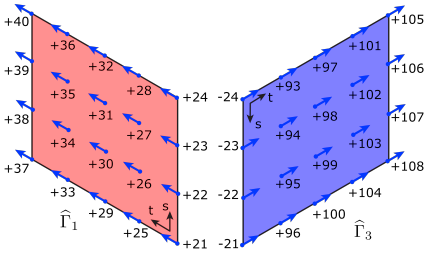

(c) Domains $\widehat{\Gamma}_1$ and $\widehat{\Gamma}_3$.

Figure 6: Example div-conforming vector basis connectivity associated with the NURBS multipatch geometry shown in Figure 5 for a B-spline vector basis of order $(4,3)\times(3,4)$. Red and blue arrows indicate a vector basis aligned in the s and t parametric directions respectively.

4.1. Radar Cross Section

The radar cross section σ which quantifies how detectable an object is to a radar signal in a given direction is computed as

$$\sigma = \lim_{R\to\infty} 4\pi R^2 \frac{|\mathbf{E}^s|^2}{|\mathbf{E}^i|^2} \tag{37}$$

where R is the distance between the radar signal and the target object and furthermore, it can be assumed in the present work that $|\mathbf{E}^i| = 1$. As detailed in [26, 27] if the source and field points are located far apart then $R \approx |\mathbf{x}|$ and the scattered electric field at a source (observation) point can be expressed as

$$\mathbf{E}^s(\mathbf{x}) = -\frac{j\omega\mu}{4\pi}\frac{e^{-jk|\mathbf{x}|}}{|\mathbf{x}|}\int_{\Gamma_y} \mathbf{J}(\mathbf{y}) e^{jk\mathbf{d}\cdot\mathbf{y}}\,\mathrm{d}\Gamma_y \tag{38}$$

allowing the RCS to be computed as

$$\sigma = 4\pi|\mathbf{x}|^2|\mathbf{E}^s|^2 \tag{39}$$

or, in terms of the RCS in decibels per square metre

$$\sigma_{dBsm} = 10\log_{10}\sigma. \tag{40}$$

5. Implementation

Figure 7 details the main steps in the implementation of the present method. A multipatch compatible B-spline discretization is constructed directly from the NURBS surface parameterization. The inherent link between the geometry and analysis models allows for straightforward computation of compatible basis functions with the relevant Piola transforms. We utilise Bézier extraction [28] to accelerate computations whereby high order B-spline and NURBS basis functions are computed through precomputed Bézier extraction coefficients and inexpensive Bernstein polynomials.

As is well-known with Galerkin boundary element methods, careful consideration must be given to the computation of the matrix components $\mathbf{Z}_{AB}$ given by (35) when the element domains Γ_x and Γ_y are either coincident, edge adjacent, vertex adjacent or lie close to one another. We use the robust quadrature algorithms proposed by Sauter and Schwab [29] that deal with each of these cases. Our implementation applies a quadrature rule of $(p+1)$ quadrature points in each parent coordinate direction for both outer and

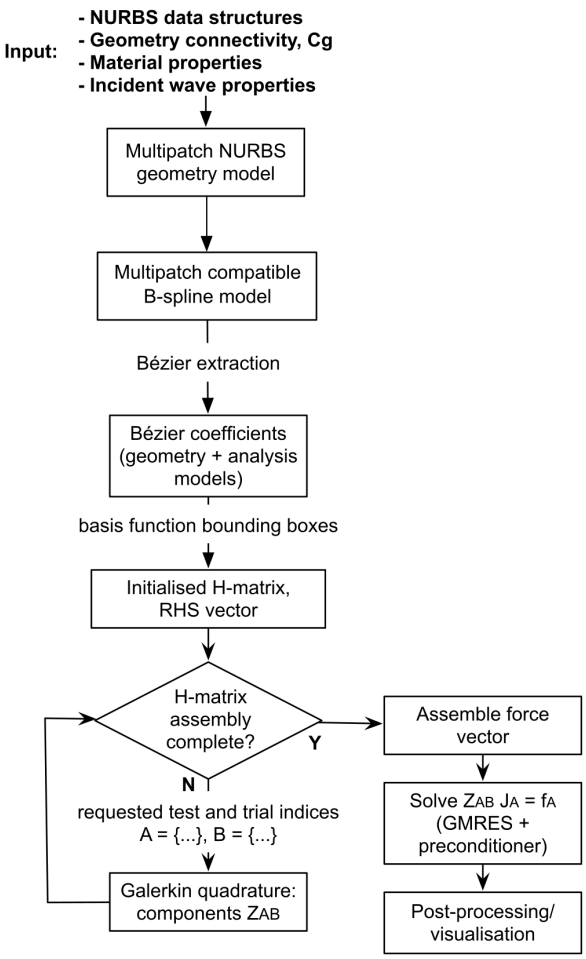

Figure 7: An outline of the algorithm for performing electromagnetic scattering with compatible B-splines using the boundary element method with $\mathscr{H}$-matrix acceleration and Bézier extraction.

inner boundary integrals. This strategy is non-optimal, particularly in the case of high order discretizations and further studies are required to optimize quadrature which is particularly important for reducing the matrix assembly process that dominates runtime. One possible route for quadrature optimization is to take advantage of the tensor product structure as demonstrated by [30]. We also point out that in comparison to standard BE discretizations the scaling behaviour of matrix assembly runtimes will be identical in terms of the number of elements (assuming identical quadrature routines are applied) with small differences attributable to the cost of evaluating basis function terms (e.g. Bernstein versus Lagrange polynomials).

To overcome the debilitating nature of the large dense matrix $\mathbf{Z}$, we approximate this matrix using $\mathscr{H}$-matrices whereby a low-rank approximation is constructed through appropriate geometrical cluster trees that separate terms into admissible and non-admissible terms (i.e. far-field and near-field terms respectively). We do not wish to delve into the technical details of $\mathscr{H}$-matrices and instead guide the reader to relevant literature (see e.g. [31, 32]). However, we remark that $\mathscr{H}$-matrices are found to be particularly amenable for implementation into an existing BEM library and we make use of the library HLibPro [33] which provides high-performance $\mathscr{H}$-matrix libraries that scale optimally over multicore hardware and are primarily based on the Adaptive Cross Approximation algorithm [34]. The library requires as an input the set of bounding boxes defined by the support of each basis function (see Figure 8) and the basis function index associated with each box. Once an $\mathscr{H}$-matrix approximation is formed for a particular wavenumber, the matrix can be written and read freely from file which allows for highly efficient radar cross section computations. We note that this approach is valid for low to medium wavenumbers with special techniques required for high wavenumbers (e.g. [35]). For all examples considered in the present study an $\mathscr{H}$-matrix approximation was generated using the ACA algorithm with a tolerance of $\varepsilon_m = 10^{-8}$, and a GMRES iterative solver was used with an LU preconditioner and a specified tolerance of $\varepsilon_s = 10^{-8}$.

Additionally, it is well known that in the case of very low or very high frequencies the EFIE suffers from ill-conditioning requiring special preconditioners which we do not consider in the present study.

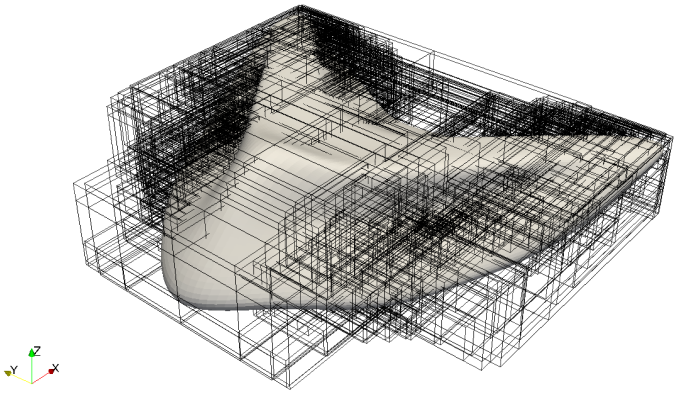

Figure 8: Example geometry with the corresponding set of bounding boxes defined by the support of each basis function used for low rank $\mathscr{H}$-matrix approximations.

6. Numerical results

To verify the present approach and to demonstrate the capability of the method of performing electromagnetic scattering directly from CAD models using an isogeometric approach we present numerical results for a series of electromagnetic scattering problems with PEC conditions.

6.1. PEC sphere

The first problem we consider is that of electromagnetic plane wave impinging on a PEC sphere of radius $a = 1$ which has a well-known solution given by the Mie series (see e.g. [22]). The incident wave is polarized in the x-direction by specifying $\mathbf{p} = (1, 0, 0)$ and is chosen to propagate in the positive z-direction with $\mathbf{d} = (0, 0, 1)$. The solution for the surface current given in spherical coordinates (ρ, θ, ϕ) (see Figure 10) is expressed as

$$
\begin{aligned}
J_\rho =& 0 \\
J_\theta =& \frac{j}{\eta} p_x \frac{\cos\phi}{ka} \sum_{n=1}^{\infty} a_n \left(\frac{\sin\theta P_n^{1'}(\cos\theta)}{\hat{H}_n^{(2)'}(ka)} + \frac{j P_n^1(\cos\theta)}{\sin\theta \hat{H}_n^{(2)}(ka)} \right) \\
J_\phi =& \frac{j}{\eta} p_x \frac{\sin\phi}{ka} \sum_{n=1}^{\infty} a_n \left(\frac{P_n^1(\cos\theta)}{\sin\theta \hat{H}_n^{(2)'}(ka)} - \frac{\sin\theta P_n^{1'}(\cos\theta)}{j \hat{H}_n^{(2)}(ka)} \right)
\end{aligned}
$$

with

$$a_n = \frac{j^{-n}(2n+1)}{n(n+1)} \tag{41}$$

where $\eta = \sqrt{\mu/\varepsilon}$, the terms P_n^1 and $P_n^{1'}$ correspond to the set of order 1 associated Legendre polynomials and derivatives respectively and

$$\hat{H}_n^{(2)} = kh_n^{(2)} \tag{42}$$

$$\hat{H}_n^{(2)'} = \left(nh_n^{(2)} - kh_{n+1}^{(2)}\right) + h_n^{(2)} \tag{43}$$

with $h_n^{(2)}$ denoting the spherical Hankel function of the second kind. The radar cross section for this problem given in terms of increasing normalized wavenumber is illustrated in Figure 9 where the two asymptotic limits associated with Rayleigh and optical scattering are labelled.

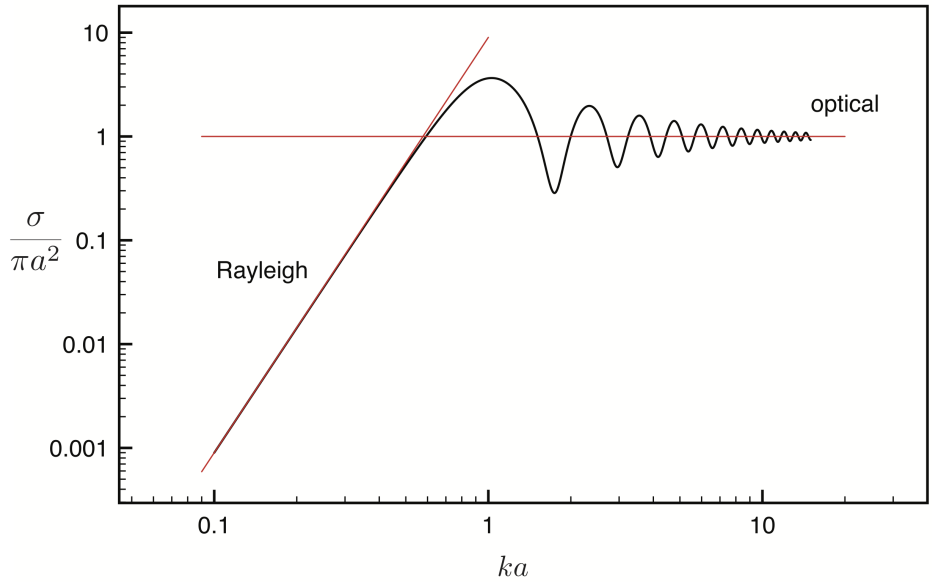

Figure 9: The monostatic radar cross section of a PEC sphere as a function of normalized wavenumber, commonly referred to as the Mie solution.

Using the present approach, the sphere geometry is discretized using biquartic NURBS patches arranged in a cube topology with no degenerate points, as in Figure 5a. Control point coordinates, weights and knot vectors for this NURBS parameterization can be found in [36]. We construct div-conforming B-splines using the knots inherited by the NURBS parameterization with degrees $(4,3)\times(3,4)$, $(3,2)\times(2,3)$, $(2,1)\times(1,2)$ and $(1,0)\times(0,1)$ and

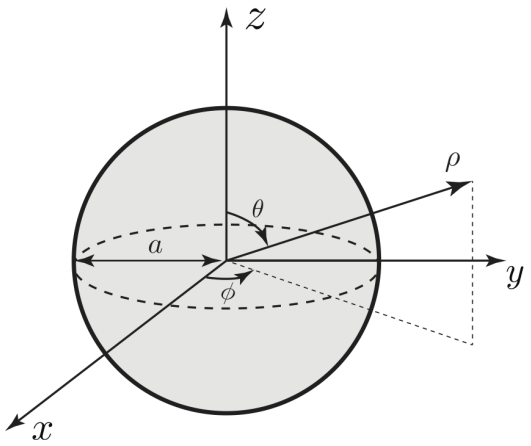

Figure 10: Mie scattering problem: spherical coordinate system.

Table 1: Details of div-conforming B-spline discretizations used in the Mie scattering study including runtimes for each order and refinement level.

mesh	**degrees of freedom (runtime (s))**			
(# elements)	$(1,0)\times(0,1)$	$(2,1)\times(1,2)$	$(3,2)\times(2,3)$	$(4,3)\times(3,4)$
h0 (6)	12 (0.13)	48 (0.62)	108 (7.93)	192 (32.0)
h1 (24)	48 (0.41)	108 (4.63)	192 (45.2)	300 (89.4)
h2 (96)	192 (5.27)	300 (10.0)	432 (127)	588 (672)
h3 (384)	768 (33.6)	972 (76.5)	1,200 (477)	1,452 (2,248)
h4 (1536)	3,072 (581)	3,468 (1,959)	3,888 (8,598)	4,332 (26,968)

apply successive h-refinement (knot insertion) to generate a set of meshes h0 (base mesh), h1, h2 etc. Table 1 provides further details of each discretization. It should be noted that compatible B-splines of degree $(1,0)\times(0,1)$ are directly equivalent to low order Raviart-Thomas or RWG basis functions on quadrilateral meshes. The bi-quartic NURBS representation of the geometry is used for all analyses and thus geometric error is eliminated for all discretizations considered.

After solving for surface current, equations (38) and (39) were used to determine radar cross section values with the results for mesh h3 shown in Figure 11 for each B-spline degree. The superior RCS accuracy obtained through higher order B-spline discretizations is demonstrated and this is also apparent in RCS values obtained with meshes h0, h1 and h2 as presented in Appendix B. As expected, finer meshes are capable of handling higher

wavenumbers.

Plots of surface currents and magnitudes for $k = 8$, h3 are shown for each B-spline degree in Figures 12 through to 15 where the higher accuracy and smoothness offered through higher B-spline degrees is visible. Recalling that the $(1,0)\times(0,1)$ discretization is equivalent to the commonly used Raviart-Thomas elements, it is clear that higher order compatible B-spline discretizations offer substantial accuracy improvements over such elements.

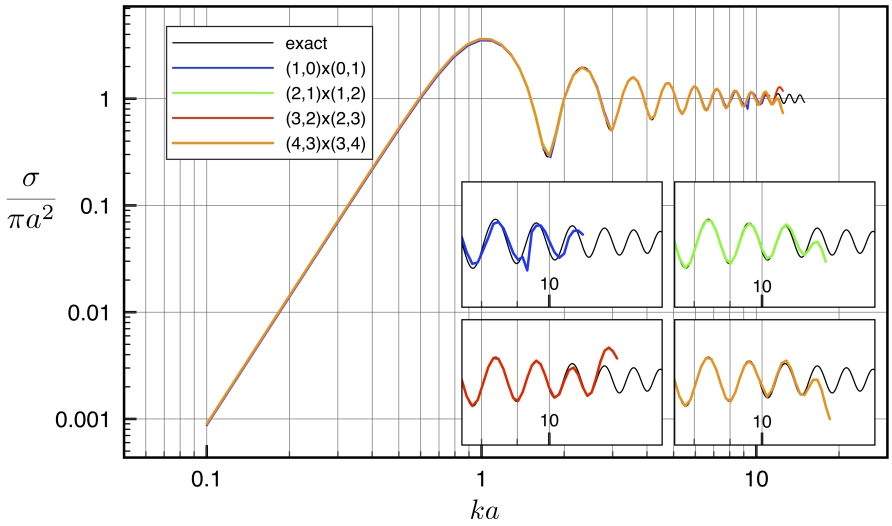

Figure 11: Normalized RCS values for a PEC sphere computed for increasing wavenumber with div-conforming B-splines of varying degree, mesh h3

Additionally, to establish that correct convergence rates are obtained using our approach we compute relative errors using the norm defined by

$$||\mathbf{v}||_{H(\mathrm{div},\Gamma)} = ||\mathbf{v}||_{L_2} + ||\mathrm{div}_\Gamma\, \mathbf{v}||_{L_2}, \tag{44}$$

where we remark that the L^2 norm of the surface divergence is well defined for this particular example. A convergence rate of $p+1$ is expected for a given B-spline degree with minimum degree p. We specify a wavenumber of $k = 3$ and evaluate relative errors through the norm of (44) for each B-spline degree for meshes h0 to h4. Relative errors for this study are plotted in Figure 16 where theoretical convergence rates are demonstrated.

Finally for this problem, we draw attention to the runtimes for each order and refinement level shown in Table 1 which were obtained on a mobile

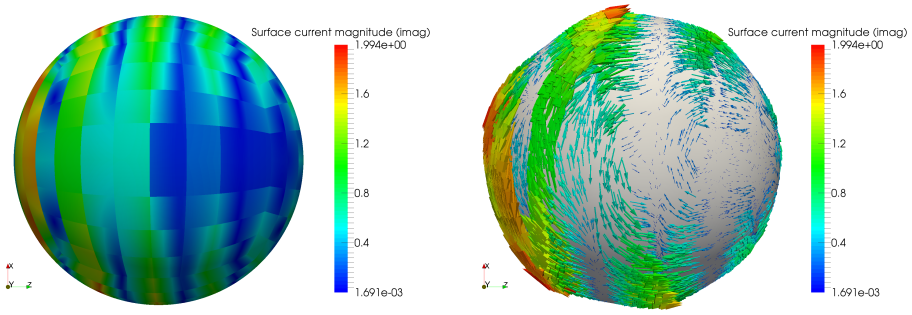

(a) $|\mathbf{J}_i|$ (b) $\mathbf{J}_i$

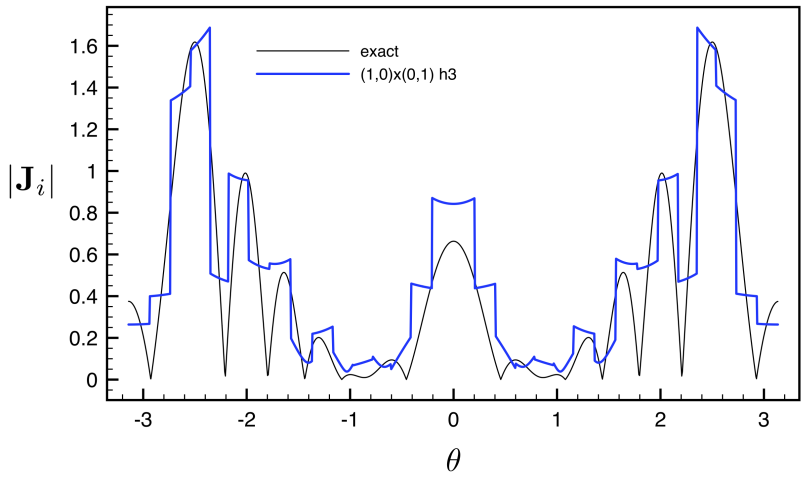

(c) $|\mathbf{J}_i|$ sampled over y - z plane.

Figure 12: Sphere scattering problem, $k = 8$: surface current quantities (imaginary component) obtained with div-conforming B-splines of degree $(1, 0)\times(0, 1)$ and three levels of h-refinement (h3).

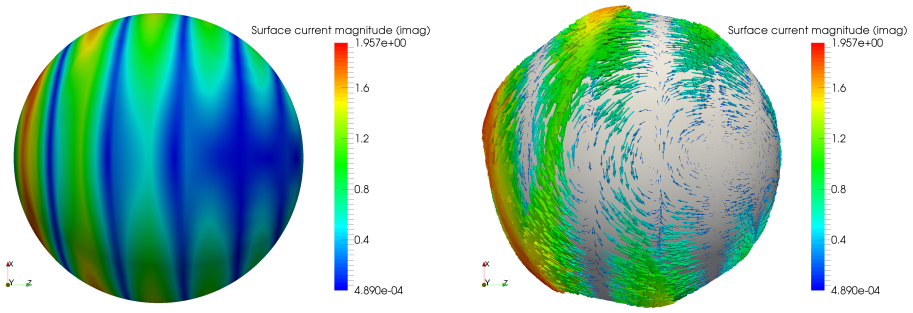

(a) $|\mathbf{J}_i|$ (b) $\mathbf{J}_i$

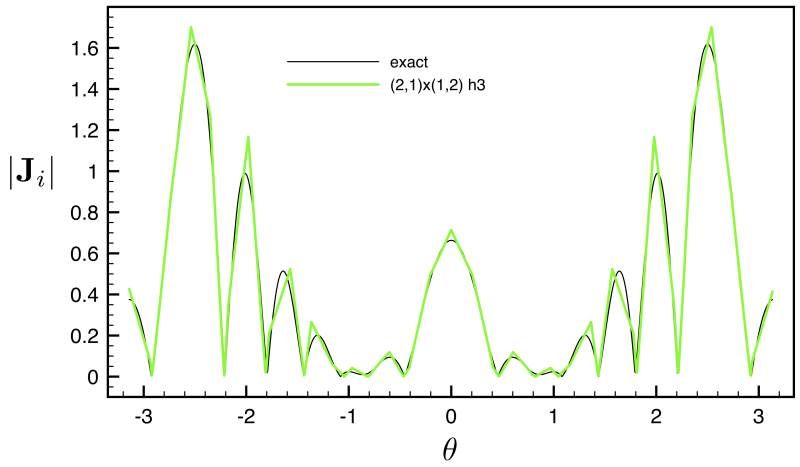

(c) $|\mathbf{J}_i|$ sampled over y - z plane.

Figure 13: Sphere scattering problem $k = 8$: surface current quantities (imaginary component) obtained with div-conforming B-splines of degree $(2, 1)\times(1, 2)$ and three levels of h-refinement (h3).

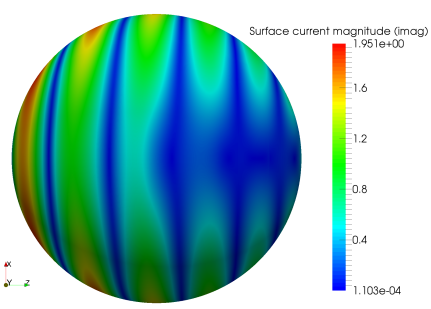

(a) $|\mathbf{J}_i|$

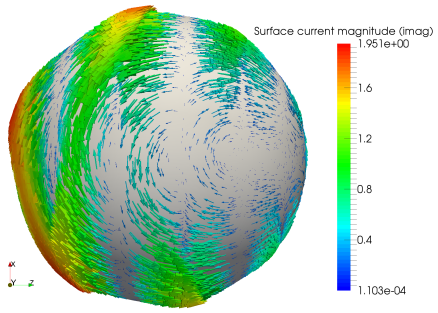

(b) $\mathbf{J}_i$

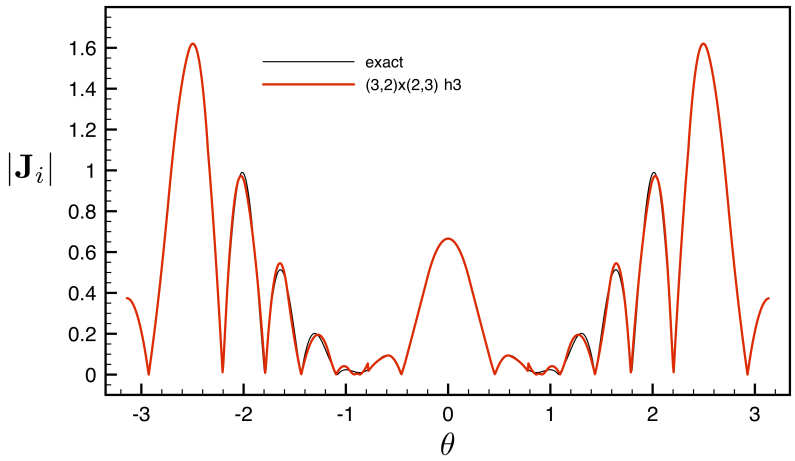

(c) $|\mathbf{J}_i|$ sampled over y - z plane.

Figure 14: Sphere scattering problem $k = 8$: surface current quantities (imaginary component) obtained with div-conforming B-splines of degree $(3, 2)\times(2, 3)$ and three levels of h-refinement (h3).

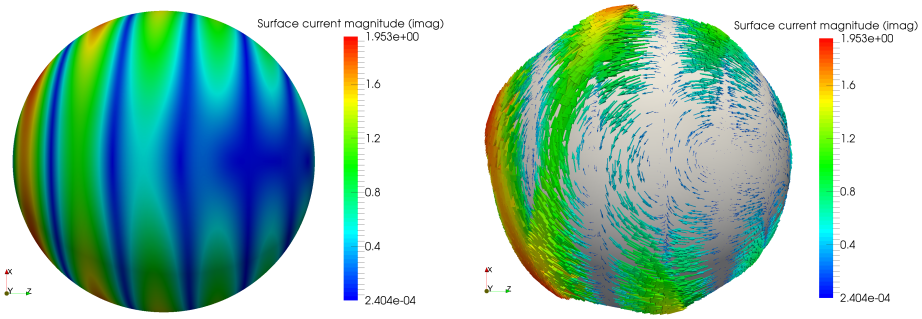

(a) $|\mathbf{J}_i|$ (b) $\mathbf{J}_i$

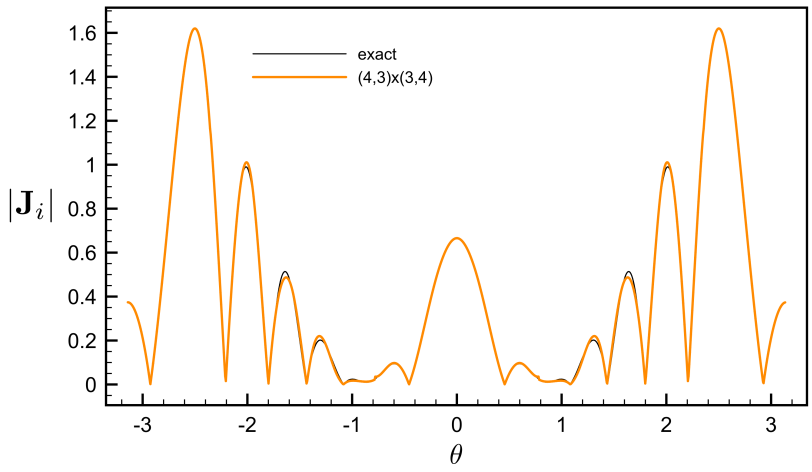

(c) $|\mathbf{J}_i|$ sampled over y - z plane.

Figure 15: Sphere scattering problem $k = 8$: surface current quantities (imaginary component) obtained with div-conforming B-splines of degree $(4, 3)\times(3, 4)$ and three levels of h-refinement (h3).

workstation with a 2.5GHz Intel Core i7 processor consisting of 4 physical cores. There is a clear price to pay for higher order discretizations with almost a factor of 50 between runtimes of orders $(1,0)\times(0,1)$ and $(4,3)\times(4,3)$ for the finest discretizations (h4) which is attributable to the double surface integral with a $(p+1)$ quadrature implementation. However, we remark that the current framework provides the flexibility to specify order depending on accuracy requirements where, for example, a low order discretization could be used to obtain fast initial results with higher orders used for more detailed analysis. We also note that to address expensive assembly procedures that arise from double surface integrals a collocation approach could be used to provide substantially faster runtimes.

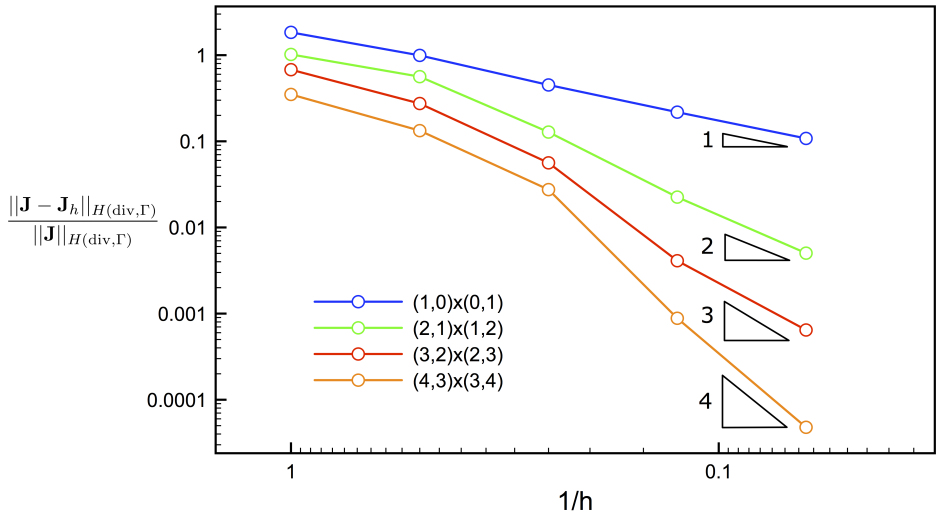

Figure 16: Mie scattering convergence study with $k = 3$: relative error norms for B-spline discretizations and theoretical convergence rates.

6.2. PEC cube

Non-smooth surfaces are found to be challenging due to the presence of non-regular solutions associated with edges and corners. We show through the example of an electromagnetic plane wave impinged on a PEC cube that the present method is capable of handling such problems. A cube is defined with unit length in each dimension centred at the origin, with a plane wave travelling in the positive x direction by specifying $\mathbf{d} = (1,0,0)$ and polarized in the z direction through $\mathbf{p} = (0,0,1)$. The entire setup is depicted in

Table 2: PEC cube study: radar cross section values for $\theta = 0$ for each B-spline order, meshes h0 to h4. The number of elements and degrees of freedom correspond exactly to that of the sphere model in Table 1.

	Backscattered RCS ($\sigma|_{\theta=0}$)			
mesh	$(1,0)\times(0,1)$	$(2,1)\times(1,2)$	$(3,2)\times(2,3)$	$(4,3)\times(3,4)$
h0	13.4160	9.5545	13.7502	13.9577
h1	8.2427	13.1235	13.1162	13.1480
h2	11.8151	13.0943	13.1801	13.2533
h3	12.8650	13.2249	13.2906	13.3195
h4	13.1738	13.3058	13.3352	13.3470

Figure 17. In keeping with the PEC cube analysis of [37] where triangular RWG and Linear-Linear basis functions are adopted, a wavenumber of $k = 2\pi$ is specified.

The geometry of the cube is constructed using one bilinear patch per face, without internal knots, for a total of 8 control points and 6 elements. Then the sets of compatible B-spline discretizations of orders $(1,0)\times(0,1)$, $(2,1)\times(1,2)$, $(3,2)\times(2,3)$ and $(4,3)\times(3,4)$ are defined by standard degree elevation. Successive h-refinement is applied to each discretization to generate a set of five meshes for each order denoted by h0 (no refinement) to h4 (4 levels of h-refinement). Figures 18a to 18d illustrate plots of $|\mathbf{J}_i|$ for each order in the mesh with two levels of h-refinement (h2) with corresponding RCS plots computed over the x-y plane in the range $\theta \in [-\pi, +\pi)$ shown in Figure 19. Table 2 states RCS values for $\theta = 0$ for all meshes, which are also plotted in Figure 20 against those obtained in [37]. Convergence to a value of $\sigma \approx 13.3$ is seen thus verifying the ability of our approach to handle non-smooth geometries. The superior accuracy of high order discretizations over low order discretizations is clearly demonstrated, and we draw attention to the fact that higher accuracies per degree of freedom are achieved for all B-spline orders in comparison to the standard BE discretizations used in [37], with the exception of the lowest order $(1,0)\times(0,1)$ compared to the Linear-Linear triangular basis.

6.3. NASA almond

A common benchmark problem used to verify electromagnetic scattering numerical methods is the NASA almond problem as detailed in [38]. The geometry of the surface is defined through parametric expressions which are

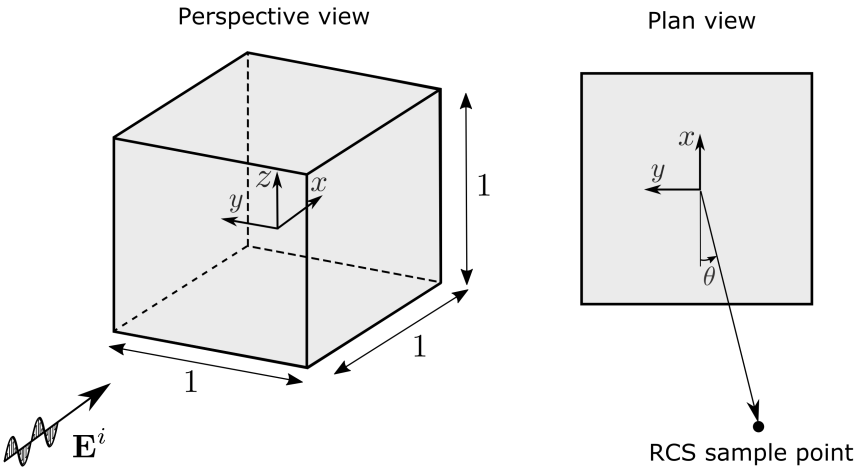

Figure 17: PEC cube study: a z-polarized electromagnetic plane wave travelling in the positive x direction impinged on a PEC cube. Sample points are defined over the x-y plane in the interval $\theta \in [-\pi, +\pi)$ with RCS values computed through (39).

detailed in Appendix C. In the present study these expressions were used as inputs to the Math Rhino plugin developed by Rhino3DE [39] generating a NURBS representation of the almond geometry with four bicubic NURBS patches as shown in Figure 21. In addition, the software library Open CASCADE [40] was used to extract the necessary geometry data structures required to construct compatible B-spline discretizations defined over the almond surface. Div-conforming B-splines of orders $(3,2)\times(2,3)$, $(2,1)\times(1,2)$ and $(1,0)\times(0,1)$ were generated with uniform h-refinement (knot insertion) applied to the initial discretization shown in Figure 21 to generate successively refined discretizations. Again, we use the notation h0, h1, h2 to indicate a mesh with no-refinement (base mesh), 1 level of h-refinement etc. and the abbreviations HH and VV to denote horizontally polarized and vertically polarized incident waves respectively. Table 3 provides further details of each B-spline discretization. For the computation of the integrals we increase the number of quadrature points in the vicinity of the two degenerate points, to increase the accuracy. We point out that the presence of a non-smooth apex in the NASA almond geometry leads to a non-regular solution.

To verify our implementation we compute the RCS given by (40) at frequencies of 1.19GHz, 3GHz and 7GHz for both horizontally and vertically

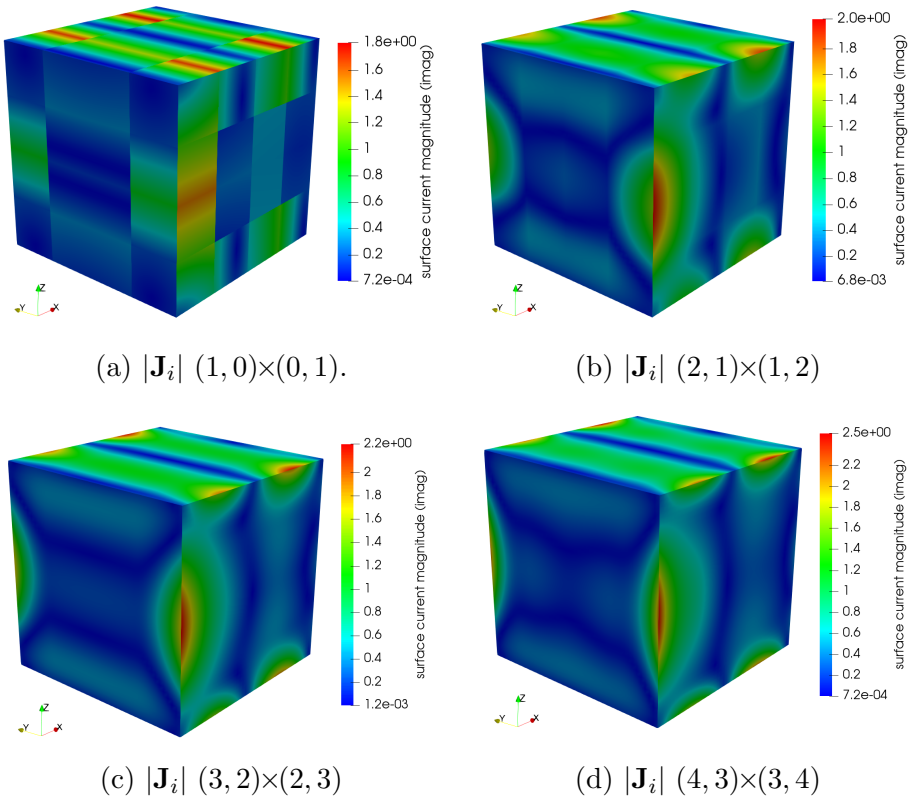

(a) $|\mathbf{J}_i|$ $(1,0)\times(0,1)$. (b) $|\mathbf{J}_i|$ $(2,1)\times(1,2)$

(c) $|\mathbf{J}_i|$ $(3,2)\times(2,3)$ (d) $|\mathbf{J}_i|$ $(4,3)\times(3,4)$

Figure 18: Surface current magnitude profiles (imaginary) for the PEC cube study defined in Figure 17 for different orders of compatible B-splines. All results correspond to meshes generated through two levels of h-refinement (h2).

Table 3: Details of compatible B-spline discretizations used for the NASA almond study.

mesh	**degrees of freedom (runtime (s))**		
(# elements)	$(1,0)\times(0,1)$	$(2,1)\times(1,2)$	$(3,2)\times(2,3)$
h0 (288)	558 (20.8)	700 (572)	858 (1,947)
h1 (1152)	2,268 (388)	2,546 (1.027e4)	2,840 (2.121e4)
h2 (4608)	9,144 (6,643)	9,694 (8.854e4)	10,260 (4.367e5)

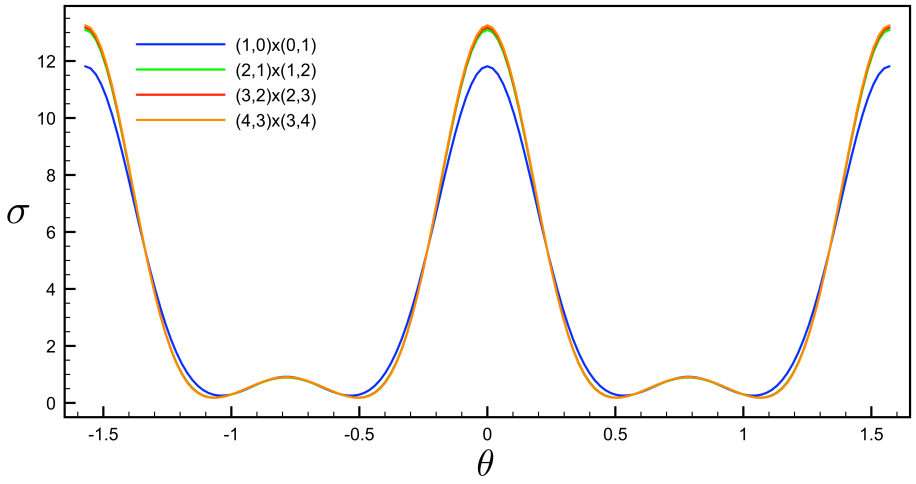

Figure 19: PEC cube RCS profiles for increasing B-spline order with 2 levels of h-refinement (h2). Values are only shown in the range $\theta \in (-\pi/2, +\pi/2]$ due to the periodicity of the solution.

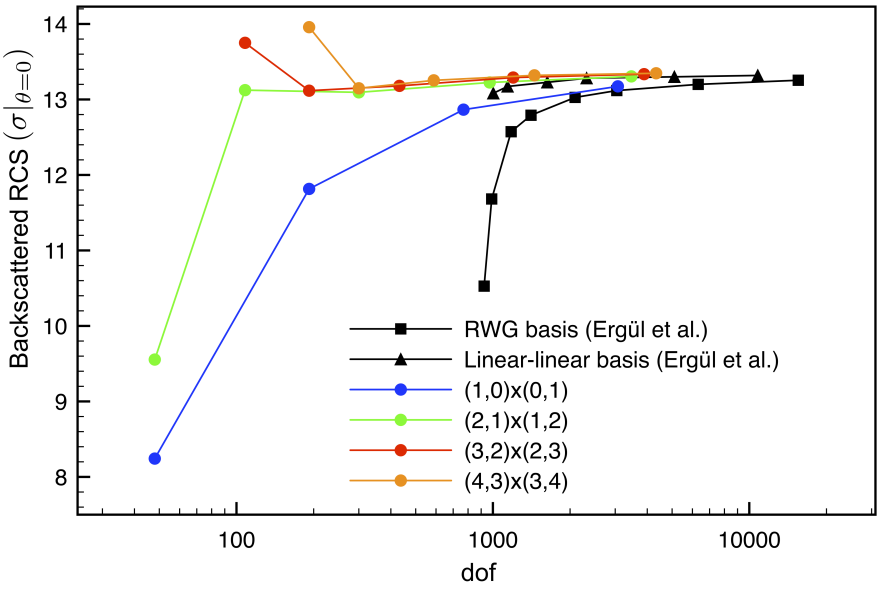

Figure 20: PEC cube study: backscattered RCS at $\theta = 0$ for increasing h-refinement compared to RCS values computed using conventional triangular discretizations obtained from [37].

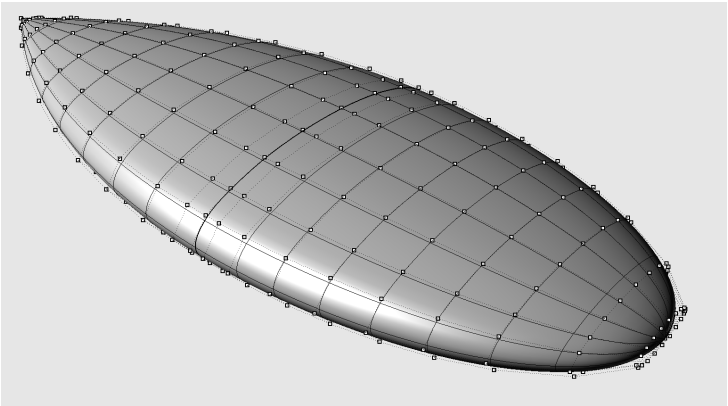

Figure 21: The NASA almond geometry represented by four bicubic NURBS patches with two degenerate points.

polarized incident waves. We use numerical RCS reference values from [41] for the 1.19GHz case, [41, 42] for the 3GHz case and [43] for the 7GHz case. In addition, we utilise experimental results for the 1.19GHz case as shown in [38]. Both [41] and [43] are based on a boundary element (method of moments) approach with the work of [42] adopting a coupled finite element/boundary element formulation.

Figure 22 illustrates RCS plots for the 1.19GHz case for each B-spline order with mesh h0. Good agreement with the numerical reference solution is visible for each order. In addition, Figure 23 demonstrates good agreement with experimental data for this frequency. In a similar manner, numerical RCS values for the 3GHz case are shown in Figure 24 where the superior accuracy of high-order discretizations is evident. Plots of the imaginary component of surface current for each order with mesh h0 are shown in Figures 25a to 25c which illustrate the smoothness in the solution obtained at higher orders.

Finally, we consider the 7GHz case where RCS plots for mesh h2 are illustrated in Figures 26 and 27 for HH and VV polarization respectively demonstrating good agreement with the numerical reference solution. At this frequency large errors were encountered for meshes h0 and h1 necessitating the use of mesh h2. Plots of the imaginary component of surface current for each order with mesh h2 are shown in Figures 28.

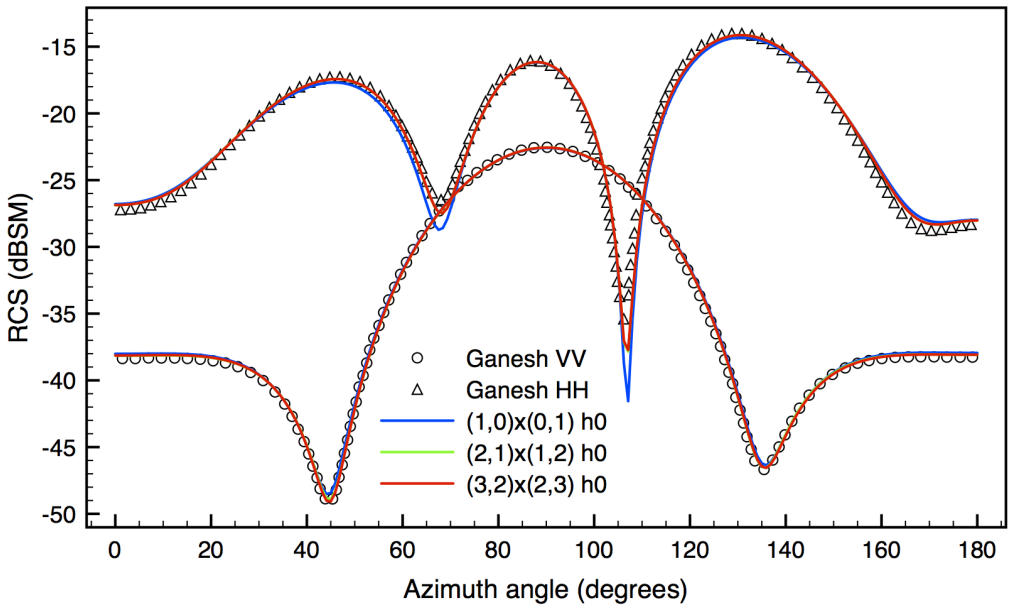

Figure 22: Radar cross section profile for NASA almond geometry: 1.19GHz, horizontal and vertical polarization. Reference data obtained from [41].

6.4. Integrated CAD and electromagnetic scattering analysis

We now demonstrate the ability of our approach to perform electromagnetic scattering analysis directly on CAD generated models. Figure 29 illustrates a concept model generated in Autodesk® Fusion 360™ which includes T-spline functionality capable of producing smooth, watertight surfaces. The model is composed of six bicubic NURBS surfaces consisting of 1,178 control points and 384 elements. By exporting this model as a STEP file which preserves all NURBS data structures and making use of the OpenCascade library, a compatible B-spline discretization is generated directly from this NURBS geometry model. We envisage a scenario where our implementation could be included directly with a CAD software library thereby eliminating this STEP file export procedure. The size of the bounding box for this model is given by $(\Delta x, \Delta y, \Delta z) = (82.3, 93.1, 27.5)$.

RCS values are computed over the x-y plane in which the wave is polarized in the z-direction. We first apply a normalized wavenumber $ka = 9.31$ and apply two levels of h-refinement (denoted by $h1$ and $h2$ respectively) using compatible B-splines of order $(3, 2)\times(2, 3)$ with normal C^0 continuity

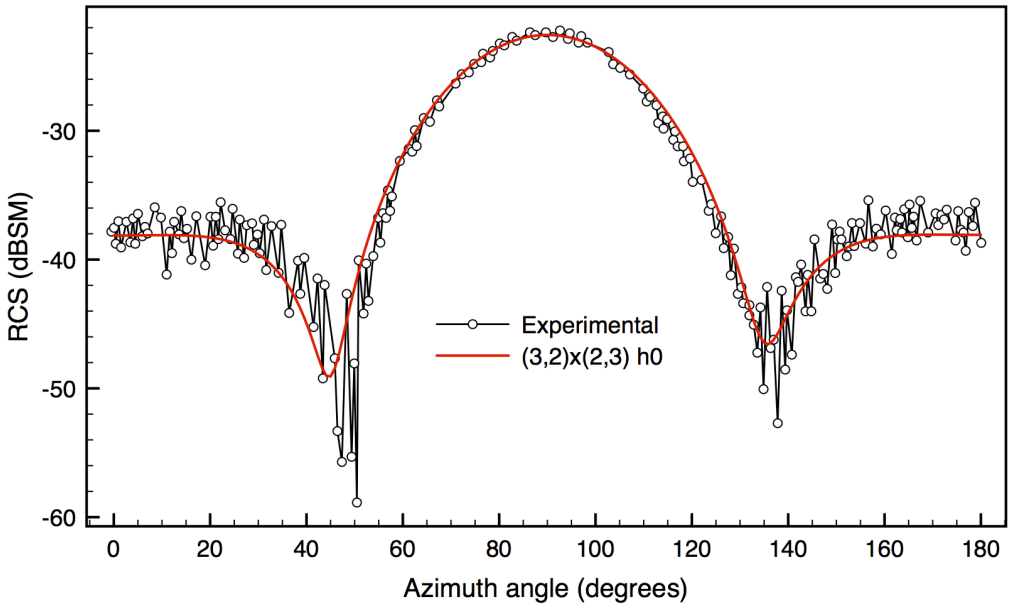

Figure 23: Comparison of experimental and numerical radar cross section profile for NASA almond geometry: 1.19GHz vertical polarization. Experimental reference data obtained from [38].

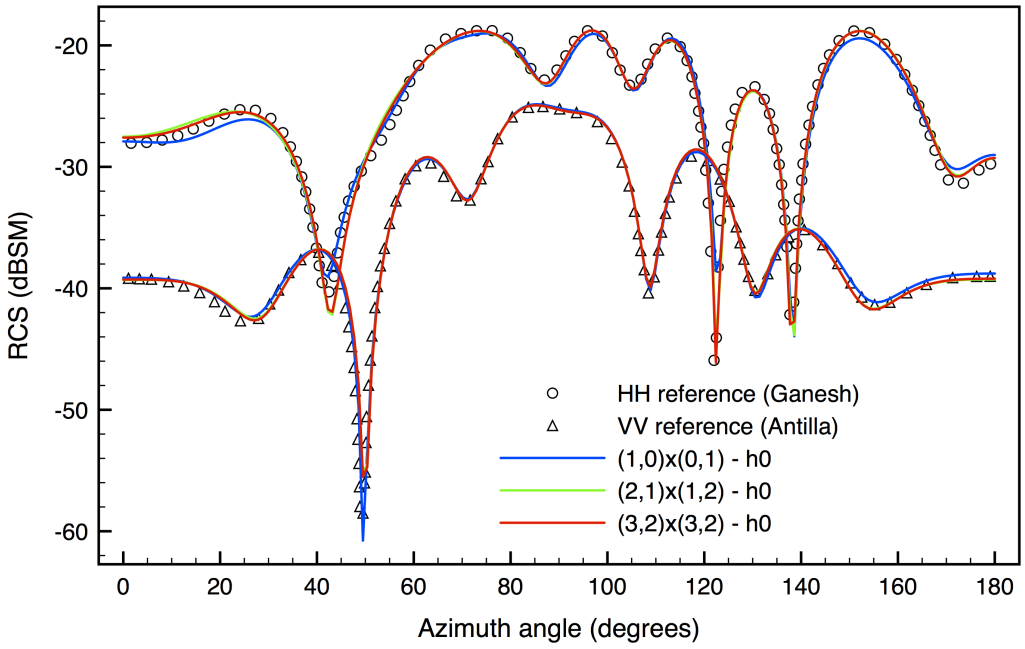

Figure 24: Radar cross section profile for NASA almond geometry: 3GHz, horizontal and vertical polarization. Reference data obtained from [41, 42].

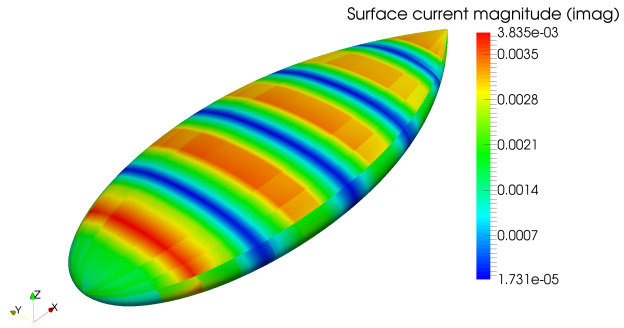

(a) Order $(1,0)\times(0,1)$.

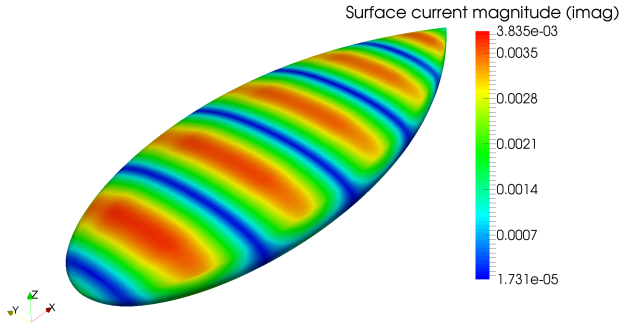

(b) Order $(2,1)\times(1,2)$.

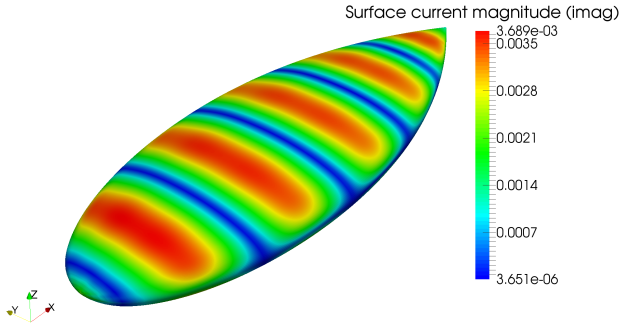

(c) Order $(3,2)\times(2,3)$.

Figure 25: Magnitude of imaginary component of surface current over the NASA almond geometry: vertically polarized planewave of 3GHz travelling in the positive $x-$direction, mesh h0.

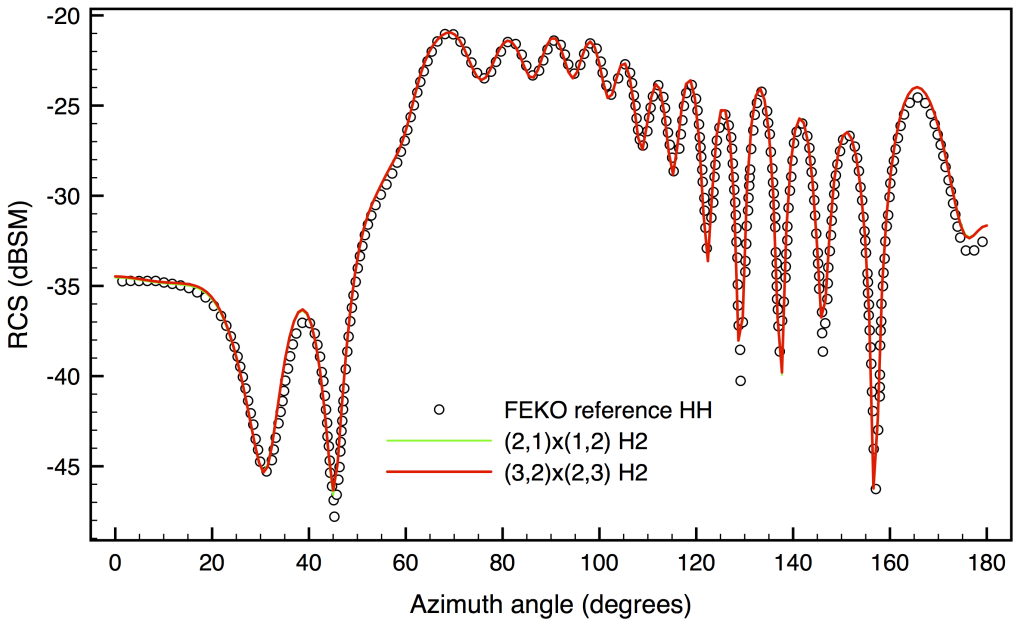

Figure 26: Radar cross section profile for NASA almond geometry: 7GHz, horizontal polarization. Reference data obtained from [43].

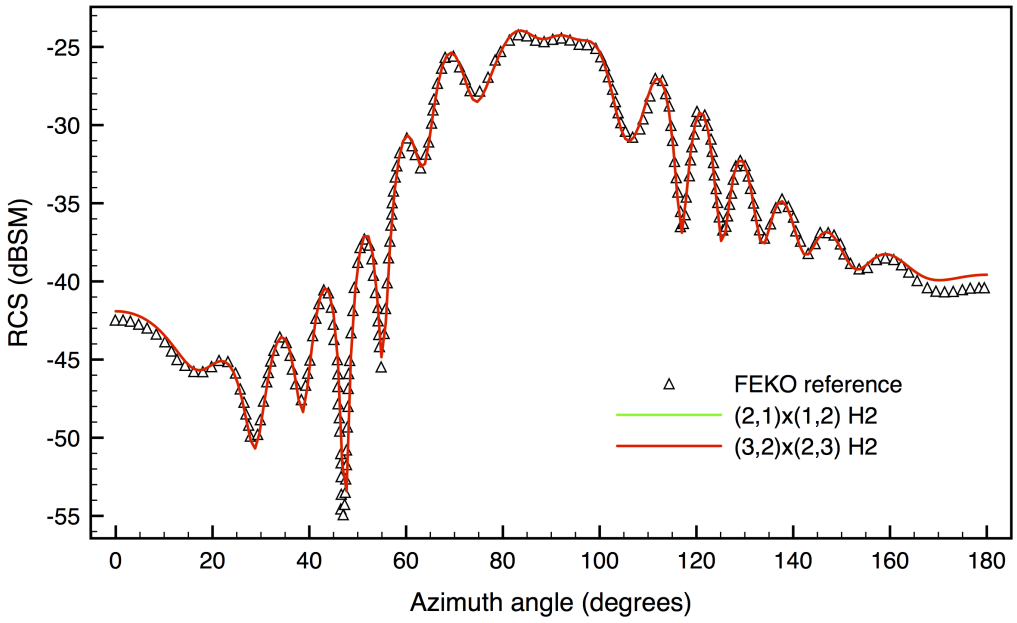

Figure 27: Radar cross section profile for NASA almond geometry: 7GHz, vertical polarization. Reference data obtained from [43].

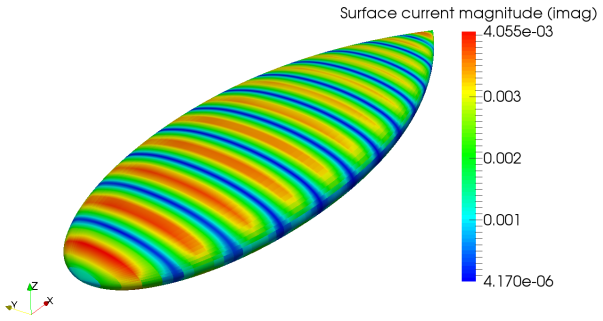

(a) $(1,0)\times(0,1)$.

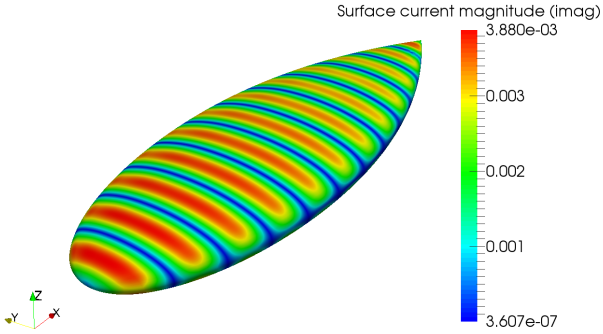

(b) $(2,1)\times(1,2)$.

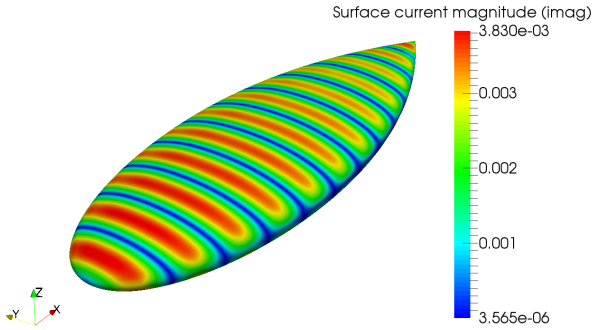

(c) $(3,2)\times(2,3)$.

Figure 28: Magnitude of imaginary component of surface current over the NASA almond geometry: vertically polarized planewave of 7GHz travelling in the positive $x-$direction, mesh h2.

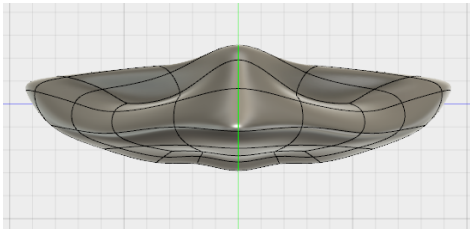

(a) Front view (y - z plane).

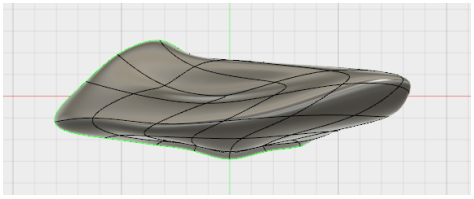

(b) Side view (x - z plane).

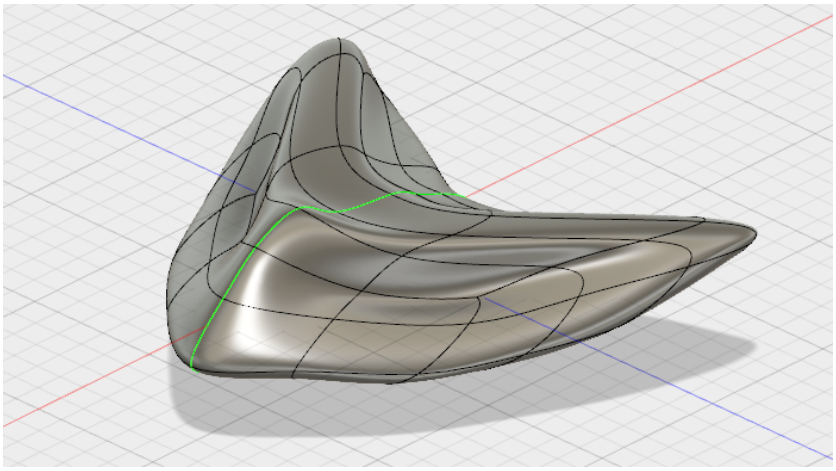

(c) Perspective view.

Figure 29: Concept model generated in Autodesk® Fusion 360™used for RCS analysis.

across patches. The discretizations $h1$ and $h2$ consist of 5,808 and 17,328 degrees of freedom respectively. Plots of the imaginary component of surface current for $h2$ are shown in Figures 30a and 30b and RCS values are plotted in Figure 31. We also compute RCS values for a higher normalized wavenumber of $ka = 46.55$ in which three levels of h-refinement are applied generating a discretization with 58,800 degrees of freedom. Surface current plots for this wavenumber are shown in Figures 32a and 32b and RCS values are plotted in Figure 33.

We use this example to demonstrate how our approach exhibits a tight link between computational design and analysis by using a common data model that provides the necessary geometry and analysis discretizations. The requirement for surface meshing is bypassed and the use of high order B-spline discretizations provides superior accuracy over conventional discretization approaches.

7. Conclusion

We have outlined an isogeometric boundary element method (method of moments) that utilises a common model to discretize both the geometry and analysis fields for electromagnetic scattering analysis. Our approach uses Non-Uniform Rational B-Splines (NURBS) to represent the surface geometry and compatible B-splines as basis for electromagnetic analysis. We have detailed the construction of compatible B-splines from a given NURBS discretization that provide a div-conforming or curl-conforming surface vector basis and described how such spline-based discretizations can be used as a basis for the electric/magnetic field integral equations. We verified our approach through the Mie series solution that provides a closed-form solution for electromagnetic scattering over a perfectly electrically conducting sphere and utilised experimental and numerical reference data for the well-known NASA almond geometry to verify radar cross section calculations. Finally, we demonstrated how our approach can be used to perform electromagnetic scattering analysis directly on geometry models generated using modern CAD software showcasing the ability of our approach to fully integrate CAD and analysis technologies.

Acknowledgements

J.A. Evans was partially supported by the Air Force Office of Scientific Research under Grant No. FA9550-14-1-0113. R. Vázquez was partially sup-

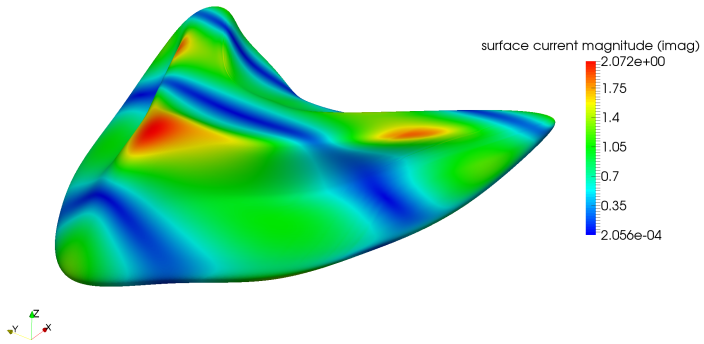

(a) $|\mathbf{J}_i|$

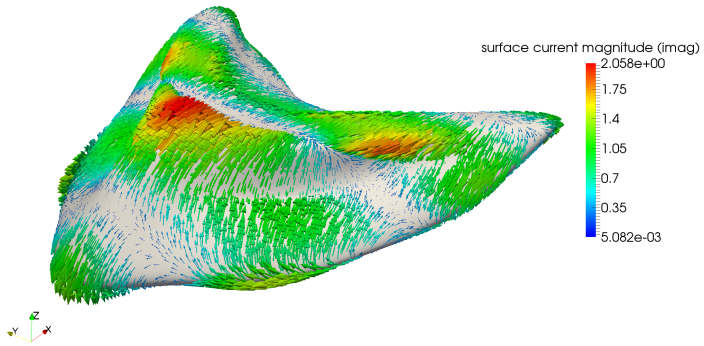

(b) $\mathbf{J}_i$

Figure 30: An example surface current profiles (imaginary) for the concept model shown in Figure 29. The plane wave is polarized in the z direction and travelling in the positive x direction with $ka = 9.31$.

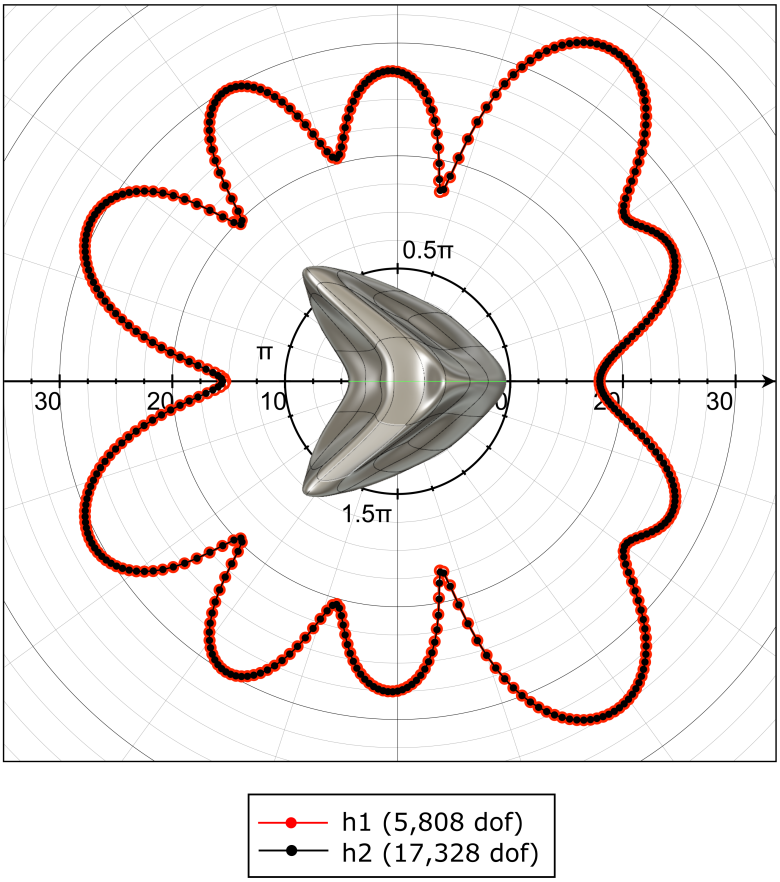

Figure 31: The computed radar cross section profile for the concept model illustrated in Figure 29 with a normalized wavenumber $ka = 9.31$.

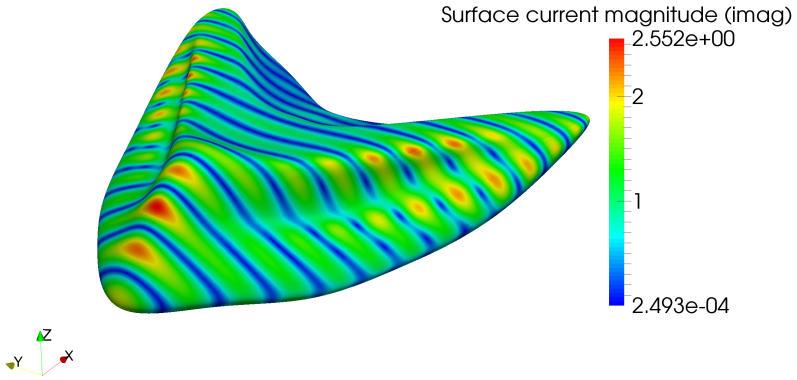

(a) $|\mathbf{J}_i|$

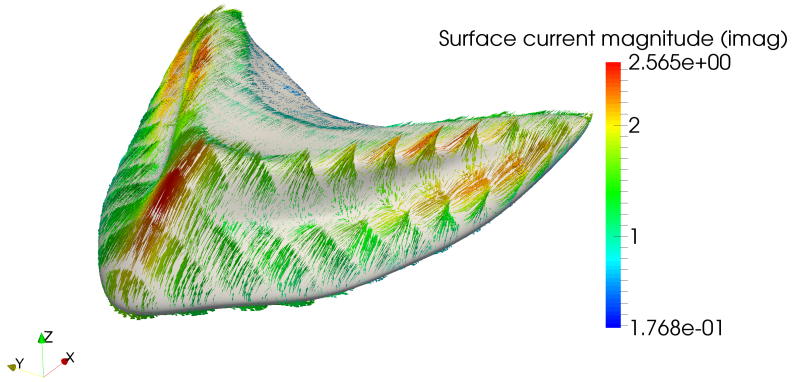

(b) $\mathbf{J}_i$

Figure 32: An example surface current profiles (imaginary) for the concept model shown in Figure 29. The plane wave is polarized in the z direction and travelling in the positive x direction with $ka = 46.55$.

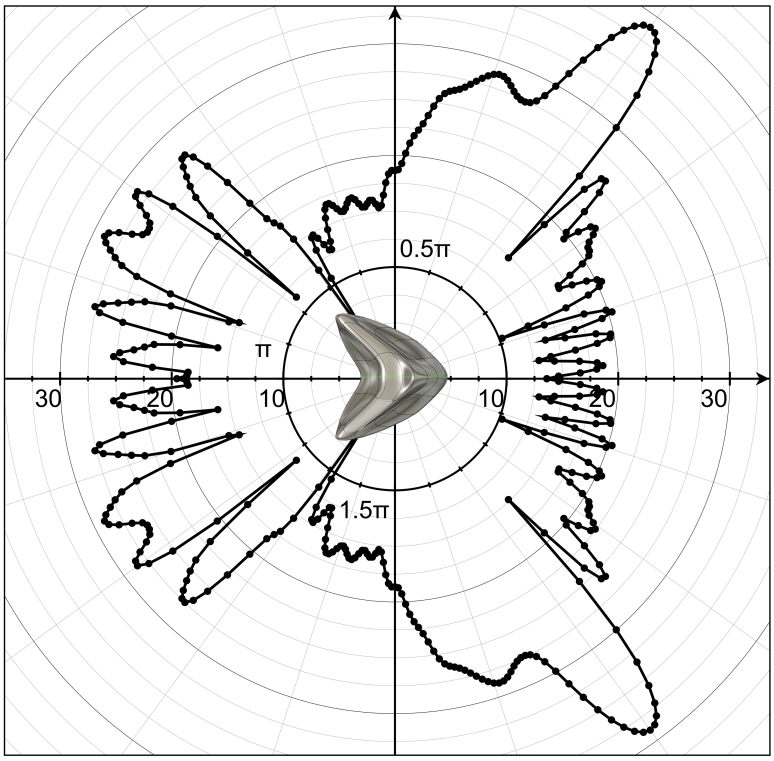

Figure 33: The computed radar cross section profile for the concept model illustrated in Figure 29 with a normalized wavenumber $ka = 46.55$.

ported by the European Research Council through the H2020 ERC Advanced Grant no. 694515 CHANGE (PI: Annalisa Buffa).

A. MFIE: compatible B-spline discretization

In a similar manner to the electric field integral equation, the magnetic field integral equation is first derived by substituting the expression for the total magnetic field given by

$$\mathbf{H} = \mathbf{H}^i + \mathbf{H}^s. \tag{45}$$

into the PEC condition of

$$\mathbf{n} \times \mathbf{H} = \mathbf{J} \tag{46}$$

to arrive at

$$\mathbf{n} \times \mathbf{H}^i = \mathbf{J} - \mathbf{n} \times \mathbf{H}^s \tag{47}$$

with the scattered magnetic field given by the quantity

$$\mathbf{H}^s = \nabla \times \mathbf{A} \tag{48}$$

allowing (47) to be rewritten as

$$\mathbf{n} \times \mathbf{H}^i = \mathbf{J} - \mathbf{n} \times \int_\Gamma \nabla \times \mathbf{J} \, \frac{e^{-jkr}}{4\pi r} \, \mathrm{d}\Gamma. \tag{49}$$

Defining the linear operator

$$L^H(\mathbf{u}) = \mathbf{u} - \mathbf{n} \times \int_\Gamma \nabla \times \mathbf{u} \, \frac{e^{-jkr}}{4\pi r} \, \mathrm{d}\Gamma \tag{50}$$

and a forcing function $\mathbf{g} = \mathbf{n} \times \mathbf{H}^i$, we write the Galerkin formulation of the magnetic field integral equation as:

given $\mathbf{g}$, find $\mathbf{J} \in H^{-\frac{1}{2}}(\mathrm{curl}_\Gamma, \Gamma)$ such that

$$\langle \mathbf{w}, L^H(\mathbf{J}) \rangle = \langle \mathbf{w}, \mathbf{g} \rangle \quad \forall \mathbf{w} \in H^{-\frac{1}{2}}(\mathrm{curl}_\Gamma, \Gamma). \tag{51}$$

Defining finite dimensional subspaces $\mathbf{w}_h, \mathbf{J}_h \in H^{-\frac{1}{2}}(\mathrm{curl}_\Gamma, \Gamma)$ as

$$\mathbf{w}_h = \sum_A^{N_b} \mathbf{N}_A^{\mathrm{curl}} w_A \tag{52}$$

$$\mathbf{J}_h = \sum_A^{N_b} \mathbf{N}_A^{\mathrm{curl}} j_A \tag{53}$$

where $\{\mathbf{N}_A^{\text{curl}}\}_{A=1}^{N_b}$ is a set of curl-conforming surface vector B-spline basis functions , the system of equations for the magnetic field integral equation can be written as

$$\mathbf{Y}_{AB}\mathbf{J}_B = \mathbf{g}_A \tag{54}$$

where, by employing the identity $\nabla \times (\phi \mathbf{v}) = \nabla\phi \times \mathbf{v} + \phi \nabla \times \mathbf{v}$, applying a limiting process to the integral and noting that $\mathbf{N}_A^{\text{div}} = -\mathbf{n} \times \mathbf{N}_A^{\text{curl}}$,

$$\mathbf{Y}_{AB} = \frac{1}{2}\int_{\Gamma_x} \mathbf{N}_A^{\text{curl}} \cdot \mathbf{N}_B^{\text{curl}}\, \mathrm{d}\Gamma + \int_{\Gamma_x} \mathbf{N}_A^{\text{div}} \cdot \left(\int_{\Gamma_y} \nabla G \times \mathbf{N}_A^{\text{curl}}\, \mathrm{d}\Gamma \right) \mathrm{d}\Gamma \tag{55}$$

where

$$\nabla G = -\frac{e^{-jkr}}{4\pi r}\left(\frac{1}{r} + jk\right)\mathbf{r} \tag{56}$$

with $\mathbf{r} := \mathbf{y} - \mathbf{x}$ and the factor of $1/2$ arises from the limiting process. Similarly, the forcing vector components are given by

$$\mathbf{g}_A = \int_{\Gamma_x} \mathbf{N}_A^{\text{curl}} \cdot (\mathbf{n} \times \mathbf{H}^i)\, \mathrm{d}\Gamma \tag{57}$$

$$= \int_{\Gamma_x} \mathbf{N}_A^{\text{div}} \cdot \mathbf{H}^i\, \mathrm{d}\Gamma. \tag{58}$$

As before, the vector $\mathbf{J}_B$ represents a vector of unknown surface current density coefficients.

B. PEC sphere - additional results

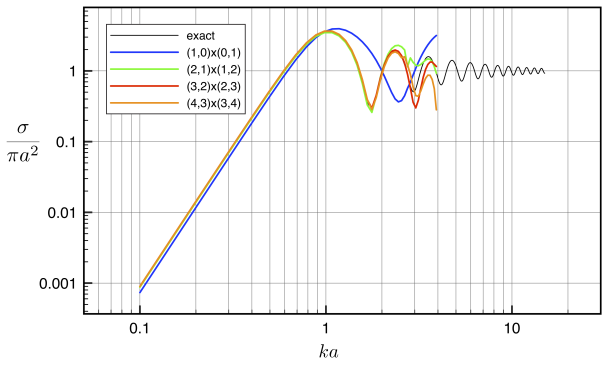

(a) h0

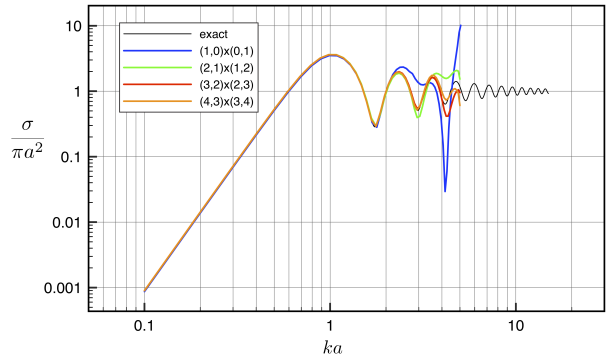

(b) h1

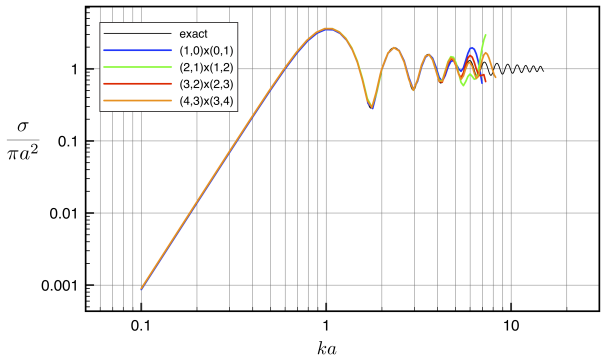

(c) h2

Figure 34: Normalized RCS values for a PEC sphere computed for increasing wavenumber with div-conforming B-splines of varying degree.

C. NASA almond geometry parameterization

Denoting the length of the almond geometry as $L = 0.2524m$, the surface of the NASA almond geometry is defined in terms of parametric coordinates (s, t) as

$$\begin{pmatrix} x \\ y \\ z \end{pmatrix} = \begin{pmatrix} Lt \\ 0.193333L\sqrt{1-\left(\frac{t}{0.416667}\right)^2}\cos s \\ 0.064444L\sqrt{1-\left(\frac{t}{0.416667}\right)^2}\sin s \end{pmatrix} \tag{59}$$
$$\text{for} -\pi < s < \pi, -0.41667 < t < 0$$

and

$$\begin{pmatrix} x \\ y \\ z \end{pmatrix} = \begin{pmatrix} Lt \\ 4.83345L\left[\sqrt{1-\left(\frac{t}{2.08335}\right)^2} - 0.96\right]\cos s \\ 1.61115L\left[\sqrt{1-\left(\frac{t}{2.08335}\right)^2} - 0.96\right]\sin s \end{pmatrix} \tag{60}$$
$$\text{for} -\pi < s < \pi, 0 < t < 0.58333.$$

[1] T. J. R. Hughes, J. A. Cottrell, Y. Bazilevs, Isogeometric analysis: CAD, finite elements, NURBS, exact geometry and mesh refinement, Computer methods in applied mechanics and engineering 194 (39) (2005) 4135–4195.

[2] Y. Bazilevs, V. M. Calo, J. A. Cottrell, J. A. Evans, T. J. R. Hughes, S. Lipton, M. A. Scott, T. W. Sederberg, Isogeometric analysis using T-splines, Computer Methods in Applied Mechanics and Engineering 199 (5) (2010) 229–263.

[3] K. A. Johannessen, T. Kvamsdal, T. Dokken, Isogeometric analysis using LR B-splines, Computer Methods in Applied Mechanics and Engineering 269 (2014) 471–514.

[4] P. Wang, J. Xu, J. Deng, F. Chen, Adaptive isogeometric analysis using rational PHT-splines, Computer-Aided Design 43 (11) (2011) 1438–1448.

[5] F. Cirak, M. Ortiz, P. Schroder, Subdivision surfaces: a new paradigm for thin-shell finite-element analysis, International Journal for Numerical Methods in Engineering 47 (12) (2000) 2039–2072.

[6] L. Liu, Y. Zhang, Y. Liu, W. Wang, Feature-preserving T-mesh construction using skeleton-based polycubes, Computer-Aided Design 58 (2015) 162–172.

[7] W. Wang, Y. Zhang, L. Liu, T. J. R. Hughes, Trivariate solid T-spline construction from boundary triangulations with arbitrary genus topology, Computer-Aided Design 45 (2) (2013) 351–360.

[8] D. J. Benson, Y. Bazilevs, M.-C. Hsu, T. J. R. Hughes, Isogeometric shell analysis: the Reissner–Mindlin shell, Computer Methods in Applied Mechanics and Engineering 199 (5) (2010) 276–289.

[9] J. Kiendl, K.-U. Bletzinger, J. Linhard, R. Wüchner, Isogeometric shell analysis with Kirchhoff–Love elements, Computer Methods in Applied Mechanics and Engineering 198 (49) (2009) 3902–3914.

[10] R. N. Simpson, S. P. A. Bordas, J. Trevelyan, T. Rabczuk, A two-dimensional isogeometric boundary element method for elastostatic analysis, Computer Methods in Applied Mechanics and Engineering 209 (2012) 87–100.

[11] K. Li, X. Qian, Isogeometric analysis and shape optimization via boundary integral, Computer-Aided Design 43 (11) (2011) 1427–1437.

[12] M. A. Scott, R. N. Simpson, J. A. Evans, S. Lipton, S. P. A. Bordas, T. J. R. Hughes, T. W. Sederberg, Isogeometric boundary element analysis using unstructured T-splines, Computer Methods in Applied Mechanics and Engineering 254 (2013) 197–221.

[13] K. V. Kostas, A. I. Ginnis, C. G. Politis, P. D. Kaklis, Ship-hull shape optimization with a T-spline based BEM–isogeometric solver, Computer Methods in Applied Mechanics and Engineering 284 (2015) 611–622.

[14] K. Bandara, F. Cirak, G. Of, O. Steinbach, J. Zapletal, Boundary element based multiresolution shape optimisation in electrostatics, Journal of Computational Physics 297 (2015) 584–598.

[15] P. A. Raviart, J. M. Thomas, A mixed finite element method for 2-nd order elliptic problems, in: Mathematical aspects of finite element methods, Springer, 1977, pp. 292–315.

[16] S. Rao, D. Wilton, A. Glisson, Electromagnetic scattering by surfaces of arbitrary shape, IEEE Transactions on antennas and propagation 30 (3) (1982) 409–418.

[17] A. Buffa, C. De Falco, G. Sangalli, Isogeometric analysis: stable elements for the 2D Stokes equation, International Journal for Numerical Methods in Fluids 65 (11-12) (2011) 1407–1422.

[18] J. A. Evans, T. J. R. Hughes, Isogeometric divergence-conforming B-splines for the steady Navier–Stokes equations, Mathematical Models and Methods in Applied Sciences 23 (08) (2013) 1421–1478.

[19] R. Vázquez, A. Buffa, Isogeometric analysis for electromagnetic problems, IEEE Transactions on Magnetics 46 (8) (2010) 3305–3308.

[20] A. Buffa, G. Sangalli, R. Vázquez, Isogeometric analysis in electromagnetics: B-splines approximation, Computer Methods in Applied Mechanics and Engineering 199 (17) (2010) 1143–1152.

[21] J. Li, D. Dault, B. Liu, Y. Tong, B. Shanker, Subdivision based isogeometric analysis technique for electric field integral equations for simply connected structures, Journal of Computational Physics 319 (2016) 145 – 162.

[22] R. F. Harrington, Time-harmonic electromagnetic fields, McGraw-Hill, 1961.

[23] L. Piegl, W. Tiller, The NURBS book, Springer, 1997.

[24] A. F. Peterson, Mapped vector basis functions for electromagnetic integral equations, Synthesis Lectures on Computational Electromagnetics 1 (1) (2005) 1–124.

[25] A. Buffa, G. Sangalli, R. Vázquez, Isogeometric methods for computational electromagnetics: B-spline and T-spline discretizations, Journal of Computational Physics 257 (2014) 1291–1320.

[26] W. C. Gibson, The method of moments in electromagnetics, Vol. 1, Chapman & Hall/CRC London, UK, 2008.

[27] C. A. Balanis, Advanced engineering electromagnetics, John Wiley & Sons, 2012.

[28] M. J. Borden, M. A. Scott, J. A. Evans, T. J. R. Hughes, Isogeometric finite element data structures based on Bézier extraction of NURBS, International Journal for Numerical Methods in Engineering 87 (1-5) (2011) 15–47.

[29] S. A. Sauter, C. Schwab, Boundary element methods, Springer, 2010.

[30] A. Mantzaflaris, B. Jüttler, B. N. Khoromskij, U. Langer, Low rank tensor methods in Galerkin-based isogeometric analysis, Computer Methods in Applied Mechanics and Engineering 316 (2017) 1062–1085.

[31] M. Bebendorf, Hierarchical matrices, Springer, 2008.

[32] W. Hackbusch, B. N. Khoromskij, R. Kriemann, Hierarchical matrices based on a weak admissibility criterion, Computing 73 (3) (2004) 207–243.

[33] R. Kriemann, HLIBpro user manual, Max-Planck-Institute for Mathematics in the Sciences, Leipzig.

[34] M. Bebendorf, Approximation of boundary element matrices, Numerische Mathematik 86 (4) (2000) 565–589.

[35] M. Bebendorf, C. Kuske, R. Venn, Wideband nested cross approximation for Helmholtz problems, Numerische Mathematik 130 (1) (2015) 1–34.

[36] J. E. Cobb, Tiling the sphere with rational Bézier patches, Tech. Rep. TR UUCS-88-009, University of Utah, USA (1988).

[37] Ö. Ergül, L. Gürel, Improving the accuracy of the magnetic field integral equation with the linear-linear basis functions, Radio Science 41 (4) (2006) 1–15.

[38] A. C. Woo, H. T. Wang, M. J. Schuh, M. L. Sanders, Benchmark radar targets for the validation of computational electromagnetics programs, IEEE Antennas and Propagation Magazine 35 (1) (1993) 84–89.

[39] Rhino3DE Math plugin, http://www.rhino3.de/_develop/__v3_plugins/math/, last accessed: 2017-01-19.

[40] Open CASCADE, https://www.opencascade.com/, last accessed: 2017-01-19.

[41] M. Ganesh, S. C. Hawkins, A spectrally accurate algorithm for electromagnetic scattering in three dimensions, Numerical Algorithms 43 (1) (2006) 25–60.

[42] G. Antilla, Radiation and scattering from curvilinear 3D composite geometries using the hybrid finite element-method of moments switch code, in: Antennas and Propagation Society International Symposium, 1994. AP-S. Digest, Vol. 1, IEEE, 1994, pp. 443–446.

[43] RCS Measurement and Simulation of Generic Simple Shapes, https://www.feko.info/product-detail/product-detail/white-papers, last accessed: 2017-01-19.